Higher-order topological phases in bilayer phononic crystals and topological bound states in the continuum

Xiao-Yu Liu,[1] Yang Liu,[1] Zhan Xiong,[2,3,*] Hai-Xiao Wang,[4,†] and Jian-Hua Jiang[1,5,‡]

[1]*School of Physical Science and Technology, and Collaborative Innovation Center of Suzhou Nano Science and Technology, Soochow University, Suzhou 215006, China*

[2]*College of Physics and Electronic Information Engineering, Zhejiang Normal University, Jinhua 321004, China*

[3]*Key Laboratory of Optical Information Detecting and Display Technology, Zhejiang Normal University, Jinhua 321004, China*

[4]*School of Physical Science and Technology, Ningbo University, Ningbo 315211, China*

[5]*Suzhou Institute for Advanced Research, University of Science and Technology of China, Suzhou 215123, China*

(Received 26 November 2023; revised 28 March 2024; accepted 2 May 2024; published 16 May 2024)

Recent studies on the interplay between band topology and the layer degree of freedom provide an effective way to realize exotic topological phases. Here we systematically study the C_6- and C_3-symmetric higher-order topological phases in bilayer spinless tight-binding lattice models. For concreteness, we consider bilayer phononic crystals as the realizations of these models. We find that for mirror-symmetric-stacking bilayer lattices the interlayer couplings control the emergence and disappearance of the topological bound states in the continuum where we consider the corner states as possible bound states in the bulk continuum. For the bilayer phononic crystals formed by two different lattices with identical symmetry, the band topology is determined by both the band topology of each layer as well as their mutual couplings. The bilayer phononic crystals experience various topological phase transitions when the interlayer couplings are gradually increased. Our paper reveals the rich physics and topological phases emerging in bilayer lattice systems that can be used to engineer interesting phenomena and topological effects.

DOI: 10.1103/PhysRevB.109.205137

I. INTRODUCTION

Exploring topological phases in phononic systems gives birth to the field of topological phononics [1–6]. Benefiting from flexibility and scalability in design and fabrication, phononic crystals provide a powerful and versatile platform to realize various topological phases, which in turn largely enrich the manipulation of the acoustic and elastic waves. Recently, the discovery of higher-order topological phases has largely expanded the classification of the topological phases of matters [7]. In contrast to the conventional topology, higher-order topology manifests itself in multidimensional topological boundary states (such as edge and corner states) beyond the conventional bulk-boundary correspondence [7]. Various higher-order topological phases, including quadruple topological insulators [8–11], octupole topological insulators [12,13], Wannier-type higher-order topological insulators [14–26], and higher-order Weyl and Dirac semimetals [27–32], have been theoretically proposed and experimentally demonstrated to host wave localization in multidimensional boundaries. For example, two-dimensional higher-order acoustic topological insulators with both gapped edge states and in-gap corner states offer an unprecedented way to realize simultaneous wave localization at the edges and corners in a dimensional hierarchy manner, which may find potential applications on topological routing of acoustic waves.

On the other hand, there has been growing interest in introducing the layer degree of freedom to topological phononics, which likely give rise to richer topological phases. The layer degree of freedom with tunable interlayer couplings provides an efficient tool to design phononic states. For example, the layer-stacking approach offers a scheme to enrich the spatial symmetry, which plays a key role in the design of three-dimensional acoustic topological insulators with Dirac hierarchy [33–37], and higher-order Weyl and Dirac semimetals [27–32]. Furthermore, the combination of the layer and valley degrees of freedom gives rise to a rich topological phase diagram, as shown in honeycomb phononic crystals [38–42]. In Lieb lattice phononic crystals, an acoustic spin-Chern insulator is proposed by introducing a layer degree of freedom with the proper interlayer coupling [43,44], in which the layer plays the role of the pseudospin degree of freedom. Very recently, it was reported that layer-stacked structures with mirror symmetry provide a useful approach to turn the boundary states of any topological monolayer model into topological bound states in the continuum [45,46]. To date, the interplay between the layer degree of freedom and the higher-order topological phases, however, remains largely unexplored, especially for bilayer structures.

To fill this gap, we systematically study the bilayer phononic crystals consisting of either identical or distinct monolayers with higher-order band topology. For instance,

*xiongzhan@zjnu.edu.cn
†wanghaixiao@nbu.edu.cn
‡jianhuajiang@suda.edu.cn

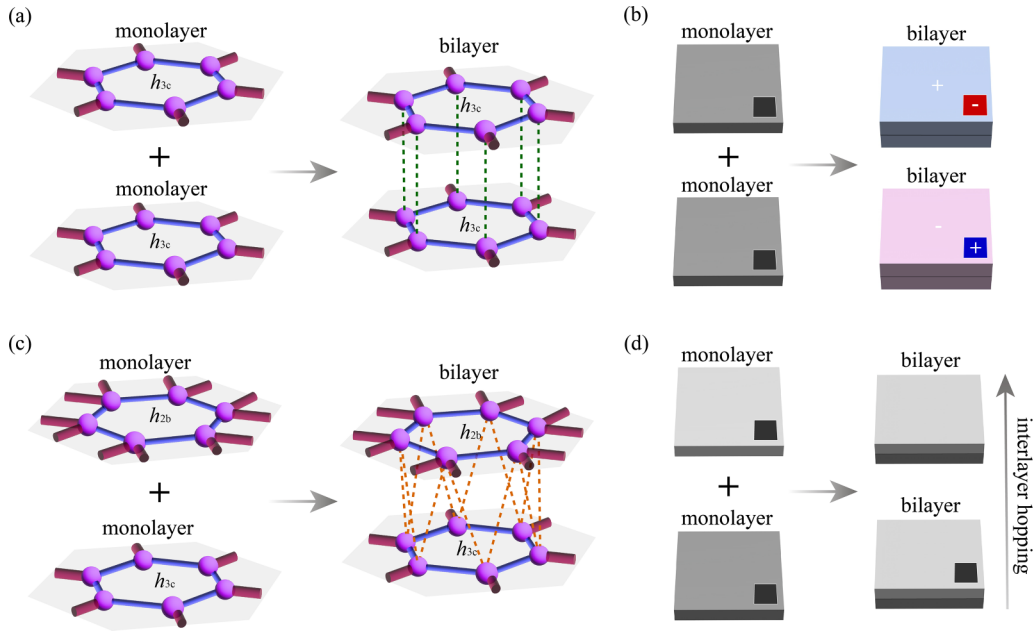

FIG. 1. (a) Bilayer phononic crystals (with mirror symmetry) formed by stacking two identical monolayers h_{3c}. (b) Mirror-stacked bilayer phononic crystals supporting two different topological bound states in the continuum. (c) Bilayer phononic crystals (without mirror symmetry) formed by stacking two distinct monolayers h_{2b} and h_{3c}. (d) Stacked bilayer phononic crystal formed by monolayers h_{2b} and h_{3c}, of which the phase transition is triggered by tuning interlayer couplings.

taking the monolayer with C_6 symmetry into consideration, there are two categories of C_6-symmetric higher-order topological insulators, labeled as $h_{2b}^{(6)}$ and $h_{3c}^{(6)}$, which are classified according to the Wannier centers of the bands below the gap [47]. When two identical monolayers, e.g., $h_{3c}^{(6)}$ and $h_{3c}^{(6)}$, are stacked together, a bilayer structure with mirror symmetry forms [see Fig. 1(a)]. Remarkably, the presence of mirror symmetry enables a classification of the states into two subspaces according to their mirror eigenvalues, i.e., even or odd. By tuning the interlayer couplings, the topological bound states in the even subspace can be tuned into the bulk continuum of the odd subspace, giving rise to the topological bound states in continuum [see sketch in Fig. 1(b)]. On the other hand, by stacking two distinct monolayers, e.g., $h_{3c}^{(6)}$ and $h_{2b}^{(6)}$, bilayer structure without mirror symmetry can be formed [see Fig. 1(c)]. In this case, by tuning the interlayer coupling, the band structure of the bilayer phononic crystal undergoes the process of band hybridization and reorganization, leading to unique topological transitions and the emergence of higher-order topological phases [see the sketched in Fig. 1(d)].

For convenience, we divide the bilayer phononic crystals into two types, according to the symmetry of layer stacking. The first type is the mirror-stacked bilayer phononic crystals that consist of two identical monolayer phononic crystals. The second type is the heterogeneous-stacked bilayer phononic crystals that consist of two monolayer phononic crystals with distinct structure and band topology. In the following sections, we will elaborate on the properties of these two types of bilayer phononic crystals. We pay special attention to the role of the interlayer couplings, the symmetry and band topology, as well as the topological bound states. Specifically, in Sec. II we study the mirror-stacked bilayer phononic crystals and the topological bound states in the bulk continuum. In Sec. III we discuss the heterogeneous-stacked bilayer phononic crystals and their band topology as well as the topological corner states. We conclude and discuss all the results as a whole in Sec. IV. In all calculations, we use the commercial finite-element software COMSOL MULTIPHYSICS to obtain the phononic dispersions and eigenstates.

II. MIRROR-STACKED BILAYER PHONONIC CRYSTALS

In this section, we focus our attention on the mirror-stacked bilayer phononic crystals and their physical results. Throughout this paper, the phononic crystals are made of cavity-tube structures. Physically, the cavity resonators mimic atomic orbitals and the narrow tubes introduce hoppings between them. Hence, cavity-tube structure-based phononic crystals provide an ideal platform to mimic the corresponding tight-binding models.

A. C_6-symmetric mirror-stacked bilayer phononic crystals formed by Wu-Hu's lattice ($h_{3c}^{(6)}$ and $h_{3c}^{(6)}$)

As a starting point, we utilize two-dimensional sixfold (C_6) rotation symmetric phononic crystals as a monolayer to work on. As shown in Fig. 2(a), the lattice constant is $a = 62$ mm. The intracell and intercell couplings are realized by the air tubes with a diameter $d_1 = 2.0$ mm and $d_2 = 4.2$ mm, respectively. Note that such a C_6-symmetric lattice with nontrivial band topology was first proposed in Ref. [48] (denoted as Wu-Hu's lattice), and has been extensively studied in the literature. Next, we constructed mirror-stacked bilayer phononic crystals by stacking the monolayer phononic crystals along z direction with distance $h_2 = 9.5$ mm [Fig. 2(b)]. By tuning the diameter d_3 of the connecting air tube, the interlayer

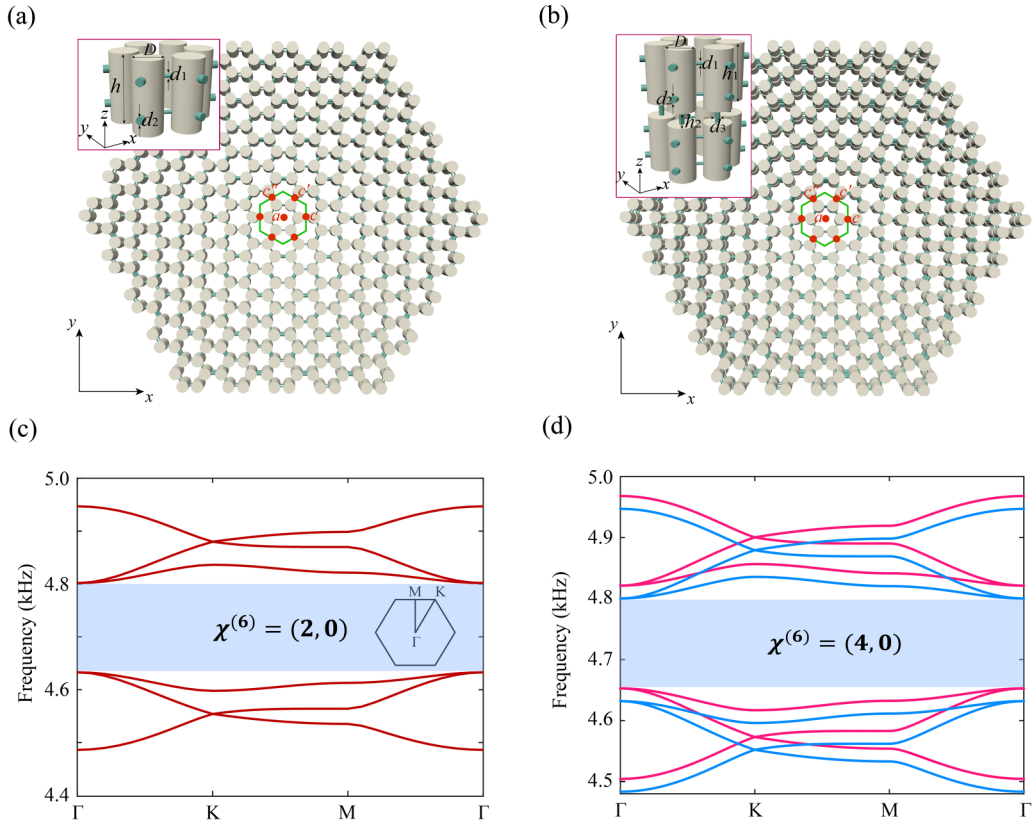

FIG. 2. (a) Schematic of monolayer phononic crystals with $h_{3c}^{(6)}$ configuration. Inset: The side view of the primitive cell. (b) Mirror-stacked bilayer phononic crystals formed by two identical monolayers with $h_{3c}^{(6)}$ configuration. (c) Band structure of monolayer phononic crystals. (d) Band structure of the mirror-stacked bilayer phononic crystals formed by two identical monolayers with $h_{3c}^{(6)}$ configuration.

coupling can be finely controlled. To characterize the band topology, we employ the topological crystalline index [47], which can be expressed by the full sets of the crystalline symmetry eigenvalues at high-symmetry points. The basic idea is to compare the rotation eigenvalues at various high-symmetry points with a reference point (the Γ point). If the eigenvalues change at these high-symmetry points, then the bands are of nontrivial topology. For instance, the C_n rotation eigenvalues of the valence bands at a high-symmetry point Π are defined as $\Pi_p^{(n)} = e^{i2\pi(p-1)/n}$ with p ranges from 1 to n. By utilizing the C_n symmetry eigenvalues at the high-symmetry point Π compared to the reference high-symmetry point Γ, an integer topological index can be defined as follows:

$$\left[\Pi_p^{(n)}\right] = \#\Pi_p^{(n)} - \#\Gamma_p^{(n)}, \tag{1}$$

where $\#\Pi_p^{(n)}(\#\Gamma_p^{(n)})$ refers to the number of bands below the band gap with the C_n symmetry eigenvalue $\Pi_p^{(n)}(\Gamma_p^{(n)})$ at the Π (Γ) point. Note that some of the topological indices are mutually dependent due to physical constraints. According to Ref. [47], the minimum set of indices that describe the band topology of the C_6 crystalline insulator is given by

$$\chi^{(6)} = \left(\left[M_1^{(2)}\right], \left[K_1^{(3)}\right]\right). \tag{2}$$

For the monolayer phononic crystal, it is seen that there are a total of six acoustic bands, and a complete band gap separates them into two groups [Fig. 2(c)]. The calculated topological indices of the monolayer phononic crystal are $\chi^{(6)} = (2, 0)$, indicating that it is of nontrivial topological property. In the view of the Wannier configuration, the Wannier centers of the lowest three bands are located at positions c, c', and c'', respectively [also see the green hexagon in Fig. 2(a)]. For convenience, we use the notation $h_{mW}^{(n)}$ to characterize the monolayer phononic crystals with C_n symmetric with m filled bands and with Wannier centers at the maximal Wyckoff position W. Hence, the monolayer phononic crystals in Figs. 2(a) and 2(c) are termed as $h_{3c}^{(6)}$. Note that such a Wannier configuration leads to a "fractional corner charge" of $\frac{1}{2}$, which is determined by the topological indices of the bulk bands as [47]

$$Q^{(6)} = \tfrac{1}{4}\left[M_1^{(2)}\right] + \tfrac{1}{6}\left[K_1^{(3)}\right] \mod 1. \tag{3}$$

For the mirror-stacked bilayer phononic crystals with $h_{3c}^{(6)}$ [Fig. 2(d)], it is seen that there are 12 bands, which according to their mirror parities can be divided into two sets. The blue (red) bandset refers to the bands with even (odd) mirror parity. Obviously, there exists an energy offset between two bandsets due to the interlayer coupling, and the band structure of each bandset is identical to that of the monolayer phononic crystal. Interestingly, the calculated topological indices (fractional corner charge) of the mirror-stacked bilayer phononic crystals are $\chi^{(6)} = (4, 0)$ ($Q^{(6)} = 0$), which can be regarded as the summation of topological indices (fractional corner charge) of two independent monolayer phononic crystals.

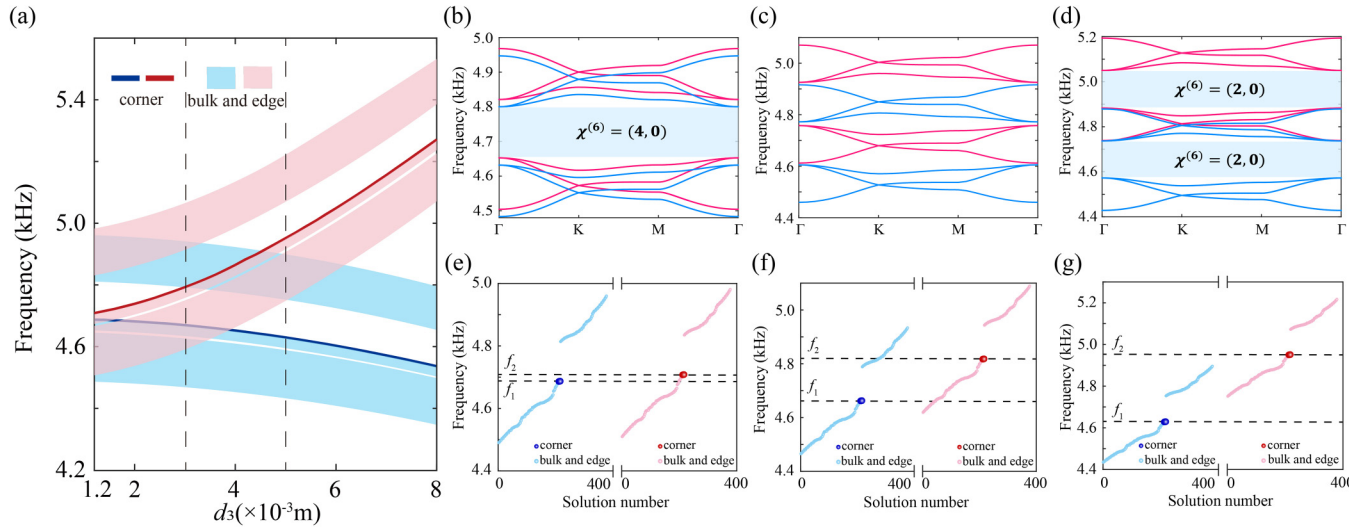

FIG. 3. (a) The eigenspectrum of mirror-stacked bilayer phononic crystals vs the diameter d_3 of the connecting air tubes. (b)–(d) The band structure of the mirror-stacked bilayer phononic crystals with diameter of the connecting air tubes (b) $d_3 = 1.2$ mm, (c) $d_3 = 3.0$ mm, and (d) $d_3 = 5.0$ mm. (e)–(g) The corresponding eigenspectrum of the mirror-stacked bilayer phononic crystals in (b)–(d), where the blue and red points refer to the acoustic states with even and odd mirror parities, respectively.

The mirror-stacked bilayer phononic crystals inherit the original band topology of the monolayer, which, in this case, is a higher-order topological phase. It is predicted that the corner states can move continuously into and out of the two-dimensional bulk continuum of opposite parity by tuning the interlayer couplings, which leads to the appearance and disappearance of the topological bound states in the continuum. To this end, we plot the energy spectra of the finite-sized mirror-stacked bilayer phononic crystals versus the diameter d_3 of the connecting air tube in Fig. 3(a). The shadow light blue (red) area and the blue (red) line refer to the bulk (edge) and corner states of mirror-stacked bilayer phononic crystals with even (odd) parity, respectively. For each subspace, it is clearly seen that the corner states emerge as the manifestation of the higher-order band topology. Remarkably, since those energetically degenerate bound and continuum states (see the overlapped areas) belong to the subspaces of different parties, hence, hybridization cannot occur between them and yield the formation of the topological bound states in the continuum. It is observed that the corner states (bound states) with odd parity emerge in the bulk states (continuum) with even parity when d_3 ranges from 3.0 to 4.5 mm, while the corner states (bound states) with even parity emerge in the bulk states (continuum) with odd parity when d_3 ranges from 1.2 to 4.0 mm.

To verify it, Figs. 3(b)–3(d) display the band structures of the mirror-stacked bilayer phononic crystals with $h_{3c}^{(6)}$ configuration, as well as the topological indices, with $d_3 = 1.2, 3.0, 5.0$ mm, respectively. As expected, accompanying the increase of the interlayer couplings, the band offset between the bandsets with even and odd mirror parities widens, and the bandset with odd (even) mirror parity move upwards (downwards). Despite the disappearance and appearance of the band gap during the band evolution, we note that the total topological indices of mirror-stacked bilayer phononic crystals remain unchanged since the topologies of the bands with different parities do not interact with each other. Accordingly, we further present the eigenspectrum of the finite-sized mirror-stacked bilayer phononic crystals in Figs. 3(e)–3(g). Note that the eigenstates with even and odd mirror parities are separately plotted, as indicated by the blue and red points. It is seen that due to the lack of the chiral symmetry, the corner states are no longer pinned at the center of the bulk gap. As shown in Fig. 3(e), when $d_3 = 1.2$ mm, the frequency of corner states with even parity enters into the frequency range of the edge states with odd parity, yielding the bound states in the edge. Meanwhile, the frequency of the corner state with odd parity is in the frequency gap of the bandset with even parity. The corresponding acoustic field patterns of two typical frequencies $f_1 = 4687$ Hz and $f_2 = 4708$ Hz, the topological bound states of which in the continuum at f_1 are highlighted by the dashed box, can be visualized in Fig. 4(a). For the case of $d_3 = 3.0$ mm in Fig. 3(f), the frequency of the corner states with even (odd) parities move to the frequency range of bulk states with odd (even) parity, yielding the two topological bound states in the continuum, which can be visualized more clearly in Fig. 4(b). Further increasing d_3 to 5.0 mm [see Fig. 3(g)], the corner states with even (odd) parity move away from the frequency range of the bandset with odd (even) parity. Hence, only topological corner states are observed for a given frequency [see the acoustic field patterns of the corner states with even and odd parities in Fig. 4(c)]. We remark that the mirror-stacking approach provides a universal way to realize topological bound states in the continuum, which have been revealed in Ref. [45].

B. C_6-symmetric mirror-stacked bilayer phononic crystals formed by a hexagonal lattice ($h_{2b}^{(6)}$ and $h_{2b}^{(6)}$)

We then proceed to discuss the mirror-stacked bilayer phononic crystals formed by stacking two identical monolayer phononic crystals with $h_{2b}^{(6)}$ configuration. As shown in Fig. 5(a), the unit cell indicated by the green hexagon consists of six cavity resonators, in which the cavity resonators are placed at the middle point of the line from the corners to

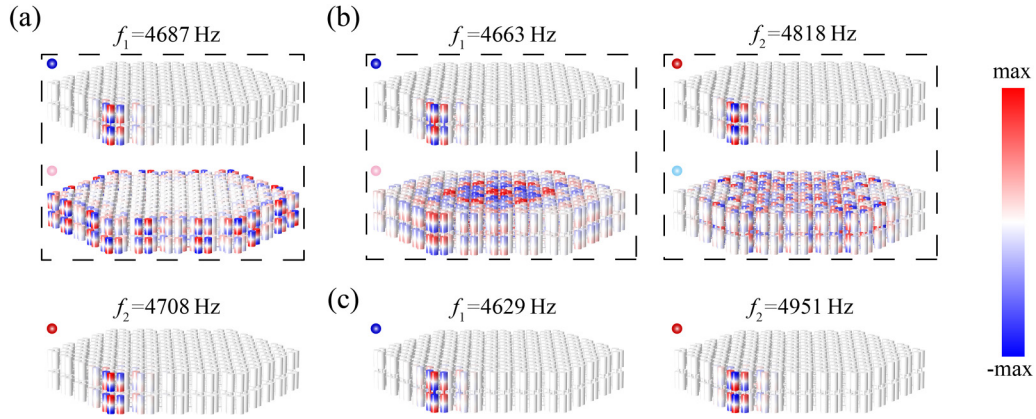

FIG. 4. (a)–(c) The corresponding acoustic pressure field patterns of mirror-stacked bilayer phononic crystals with (a) $d_3 = 1.2$ mm at frequencies of $f_1 = 4687$ Hz and $f_2 = 4708$ Hz, (b) $d_3 = 3.0$ mm at frequencies of $f_1 = 4663$ Hz and $f_2 = 4818$ Hz, and (c) $d_3 = 5.0$ mm, at frequencies of $f_1 = 4629$ Hz and $f_2 = 4951$ Hz, respectively. The topological bound states in the continuum can be visualized from those acoustic pressure field patterns in the dashed boxes.

the center of the unit cell. For simplicity, we denote it as the hexagonal lattice. Note that the topological property of the hexagonal lattice is different from that of Wu-Hu's lattice in spite of the similarity in the lattice configurations. To illustrate it, we keep all the geometric parameters of the monolayer phononic crystals in hexagonal lattice configuration the same as that in Wu-Hu's lattice configuration, namely, $H = 38$ mm and $D = 16$ mm, $d_1 = 2.0$ mm and $d_2 = 4.2$ mm. The band structure is depicted in Fig. 5(c). It is seen that there are only two bands below the gap in the hexagonal lattice, which is

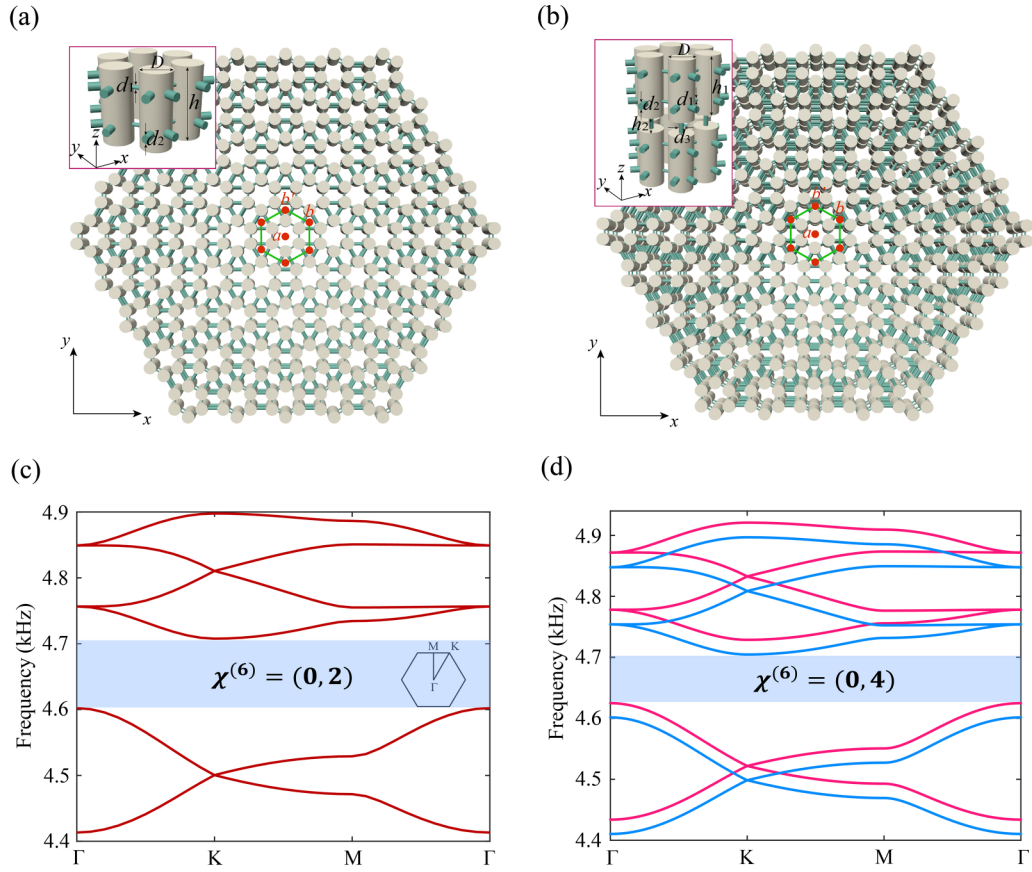

FIG. 5. (a) Schematic of monolayer phononic crystals in the configuration of a hexagonal lattice. Inset: The side view of the primitive cell. (b) The mirror-stacked bilayer phononic crystals formed by two identical monolayers in hexagonal lattice configuration. (c) Band structure of monolayer phononic crystals. (d) Band structure of the mirror-stacked bilayer phononic crystals formed by two identical monolayer phononic crystals in hexagonal lattice configuration.

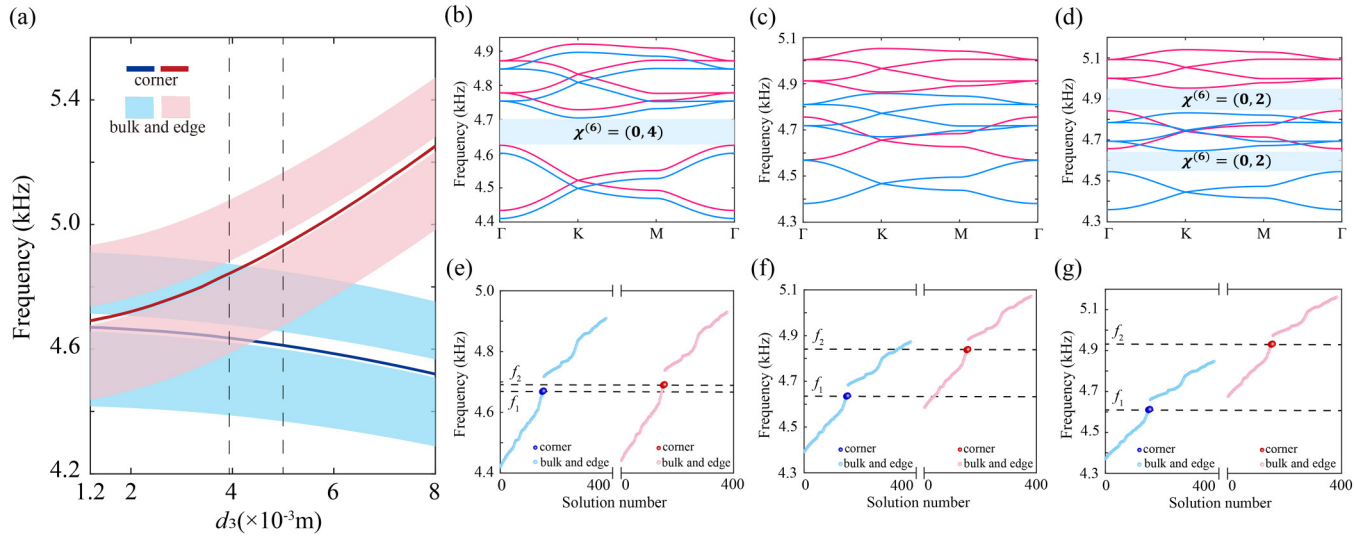

FIG. 6. (a) The eigenspectrum of mirror-stacked bilayer phononic crystals vs the interlayer coupling d_3. (b)–(d) The band structure of mirror-stacked bilayer phononic crystals with interlayer coupling (b) $d_3 = 1.2$ mm, (c) $d_3 = 3.9$ mm, and (d) $d_3 = 5.0$ mm. (e)–(g) The corresponding eigenspectrum of the mirror-stacked bilayer phononic crystals in (b)–(d), where the blue and red points refer to the acoustic states with even and odd mirror parities, respectively.

different from that in Wu-Hu's lattice configuration. Moreover, the topological indices of the first band gap give $\chi^{(6)} = (0, 2)$, indicating that such a complete band gap is of a nontrivial topological nature. In the view of the Wannier configuration, the Wannier centers of the lowest two bands are located at positions b and b', respectively [also see the green hexagon in Fig. 5(a)]. According to Eq. (3), the calculated fractional corner charge arising from the filling anomaly is $Q^{(6)} = \frac{1}{3}$.

Next, we constructed mirror-stacked bilayer phononic crystals by stacking the monolayer phononic crystals in hexagonal lattice configuration along the z direction [Fig. 5(b)]. The radii of the connecting tubes are the same as in Fig. 2(b). As shown in Fig. 5(d), it is seen that there are 12 bands, which according to their mirror parities can be divided into two sets. The blue (red) bandset refers to the bands with even (odd) mirror parity. Obviously, the interlayer coupling results in the splitting of the bands with odd and even parities. On the other hand, we notice that the calculated topological indices (fractional corner charge) of the mirror-stacked bilayer phononic crystals are $\chi^{(6)} = (0, 4)$ ($Q^{(6)} = \frac{2}{3}$), which equal to the summation of topological indices (fractional corner charge) of the monolayer phononic crystals in hexagonal lattice configuration.

Owing to the higher-order band topology in the monolayer configured with $h_{2b}^{(6)}$, it is evident that each layer structure with finite size supports six corner states in the gap. Hence, when two monolayers in hexagonal lattice configuration are placed together via mirror-stacking approach, it is expected that each layer of mirror-stacked bilayer phononic crystals hosts corner states inheriting higher-order band topology of the monolayer. Similar to the bulk band with specific mirror parity, 12 corner states in the gap are reorganized into two groups according to the mirror parities. Therefore, it is possible that the corner states can move continuously into and out of the two-dimensional bulk continuum of opposite parity by tuning the interlayer couplings, which results in the appearance and disappearance of the topological bound states in the continuum.

To this end, we plot the energy spectra of the finite-sized mirror-stacked bilayer phononic crystals versus the diameter d_3 of the connecting air tube in Fig. 6(a). The shadow light blue (red) area and blue (red) line refer to the bulk (edge) and corner states of mirror-stacked bilayer phononic crystals with even (odd) parity, respectively. For each subspace, it is clearly seen that corner states emerge as the manifestation of the higher-order band topology. Specifically, for the diameter d_3 ranges from 2.0 mm (1.2 mm) to 4.2 mm (4.4 mm), the frequency of the corner states with odd (even) parity falls into the frequency windows of the bulk states with even (odd) parity, giving rise to the topological bound states in the continuum. Since those energetically degenerate bound and continuum states belong to the subspaces of different parties, hence, hybridization cannot occur between them and yield the formation of the topological bound states in the continuum.

Moreover, Figs. 6(b)–6(d) display the band structures of the mirror-stacked bilayer phononic crystals formed by two hexagonal lattices with diameters $d_3 = 1.2, 3.9, 5.0$ mm, respectively. As expected, the band offset between the bandsets with even and odd mirror parities widens, and the bandset with odd (even) mirror parity moves upwards (downwards) accompanying the increase of the interlayer couplings. In spite of the gap closing and reopening during the band evolution, we remark that the summation of the topological indices remains unchanged owing to the fact that the topologies of two identical monolayer phononic crystals are the same but independent from each other. Accordingly, we present the eigenspectrum of finite-sized mirror-stacked bilayer phononic crystals in Figs. 6(e)–6(g). Note that the eigenstates with even and odd mirror parities are separately plotted, as indicated by the blue and red points. It is seen that due to the lack of the chiral symmetry the corner states are no longer pinned at the center of the bulk gap. As shown in Fig. 6(e), when $d_3 = 1.2$ mm, the frequency of corner states with even parity enters

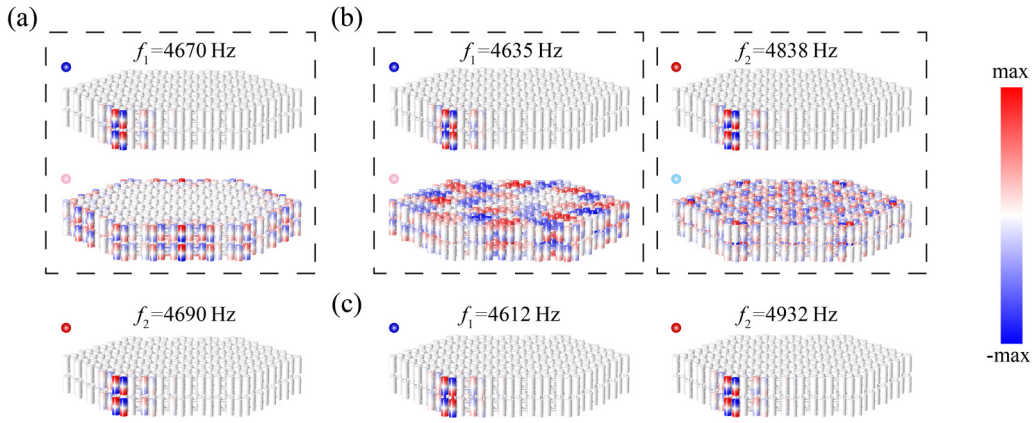

FIG. 7. (a)–(c) The corresponding acoustic pressure field pattern of mirror-stacked bilayer phononic crystals with (a) $d_3 = 1.2$ mm at frequencies of $f_1 = 4670$ Hz and $f_2 = 4690$ Hz, (b) $d_3 = 3.9$ mm at frequencies of $f_1 = 4635$ Hz and $f_2 = 4838$ Hz, and (c) $d_3 = 5.0$ mm at frequencies of $f_1 = 4612$ Hz and $f_2 = 4932$ Hz, respectively. The topological bound states in the continuum can be visualized from those acoustic pressure field patterns in the dashed boxes.

into the frequency range of the edge states with odd parity, yielding the bound states in the edge [also see the corresponding acoustic field pattern at a frequency of $f_1 = 4670$ Hz in the dashed box of Fig. 7(a)]. Meanwhile, the frequency of the corner states with odd parity is in the frequency gap of the bandset with even parity [also see the corresponding acoustic field pattern at a frequency of $f_1 = 4690$ Hz in Fig. 7(a)]. For the case of $d_3 = 3.9$ mm in Fig. 6(f), the frequency of the corner states with even (odd) parities, namely, $f_1 = 4635$ Hz ($f_2 = 4838$ Hz), falls into the frequency range of bulk states with odd (even) parity, yielding the topological bound states in the continuum, which can be visualized more clearly from the acoustic field patterns in the dashed box in Fig. 7(b). Further increasing d_3 to 5.0 mm [see Fig. 6(g)], the frequency of the corner states with even (odd) parity, namely, $f_1 = 4612$ Hz ($f_2 = 4932$ Hz), is in the frequency gap of the bandset with odd (even) parity [see the acoustic field pattern of the corner states with even and odd parities in Fig. 7(c)]. It is believed that the mirror-stacking approach provides a universal way to realize topological bound states in the continuum.

C. C_3-symmetric mirror-stacked bilayer phononic crystals formed by an upward kagome lattice ($h_{1b}^{(3)}$ and $h_{1b}^{(3)}$)

Following the above procedures, we move to discuss mirror-stacked bilayer phononic crystals formed by stacking monolayer phononic crystals with C_3 symmetry. We first discuss the mirror-stacked bilayer phononic crystals formed by stacking two identical monolayers in kagome lattice configuration. As shown in Fig. 8(a), each unit cell is made up by three cavity resonators, which are aligned with upward triangular shape. For simplicity, we denoted as upward kagome lattice. The geometric parameters of the unit cell are as follows: the diameter of the connecting air tube within the unit cell is $d_1 = 2.4$ mm, and that between two nearby unit cells is $d_2 = 4.6$ mm. The height and diameter of the individual cavity are $h_1 = 38$ mm and $D = 20$ mm. The band structure of the monolayer phononic crystal in upward kagome lattice configuration in Fig. 8(c) shows that there is only a single band below the band gap. We further characterize the band topology by utilizing the topological crystalline index. The minimum set of indices that describe the band topology of the C_3-symmetric crystalline insulator is given by [47]

$$\chi^{(3)} = \left([K_1^{(3)}], [K_2^{(3)}]\right). \tag{4}$$

The calculated topological indices of the monolayer phononic crystal in upward kagome lattice configuration are $\chi^{(3)} = (1, -1)$, indicating that it is of nontrivial topology. In the view of the Wannier configuration, the Wannier center of the lowest band is located at position b [also see the green hexagon in Fig. 8(a)]. Hence, such a monolayer is of $h_{1b}^{(3)}$ configuration. Note that such a Wannier configuration leads to a fractional corner charge of $\frac{2}{3}$, which is determined by the topological indices of the bulk bands as [47]

$$Q^{(3)} = \tfrac{1}{3}[K_2^{(3)}] \mod 1. \tag{5}$$

By stacking the monolayer phononic crystals along the z direction, as depicted in Fig. 8(b), a C_3-symmetric mirror-stacked bilayer phononic crystals form. The diameter of the connecting tube between two layers is given by d_3, which is originally set as 1.2 mm. Figure 8(d) depicts the band structure of the C_3-symmetric mirror-stacked bilayer phononic crystals. It is seen that there are six bands, which according to their mirror parities can be divided into two sets. The blue (red) bandset refers to the bands with even (odd) mirror parity. Obviously, the interlayer coupling results in the splitting of the bands with odd and even parities. The calculated topological indices of the first gap give $\chi^{(3)} = (2, -2)$, which are the summation of topological indices of two identical monolayer phononic crystals. Accordingly, the fractional corner charge gives $\frac{1}{3}$.

Owing to the higher-order band topology in the monolayer phononic crystals, it is evident that each layer structure with finite size supports three corner states in the gap. When two monolayer phononic crystals are placed together via mirror-stacking approach, each layer also hosts corner states that inherit higher-order band topology of the monolayer. Similar to the bulk band with specific mirror parity, six corner states in the gap are reorganized into two groups according to their mirror parities. Therefore, it is possible that the corner states

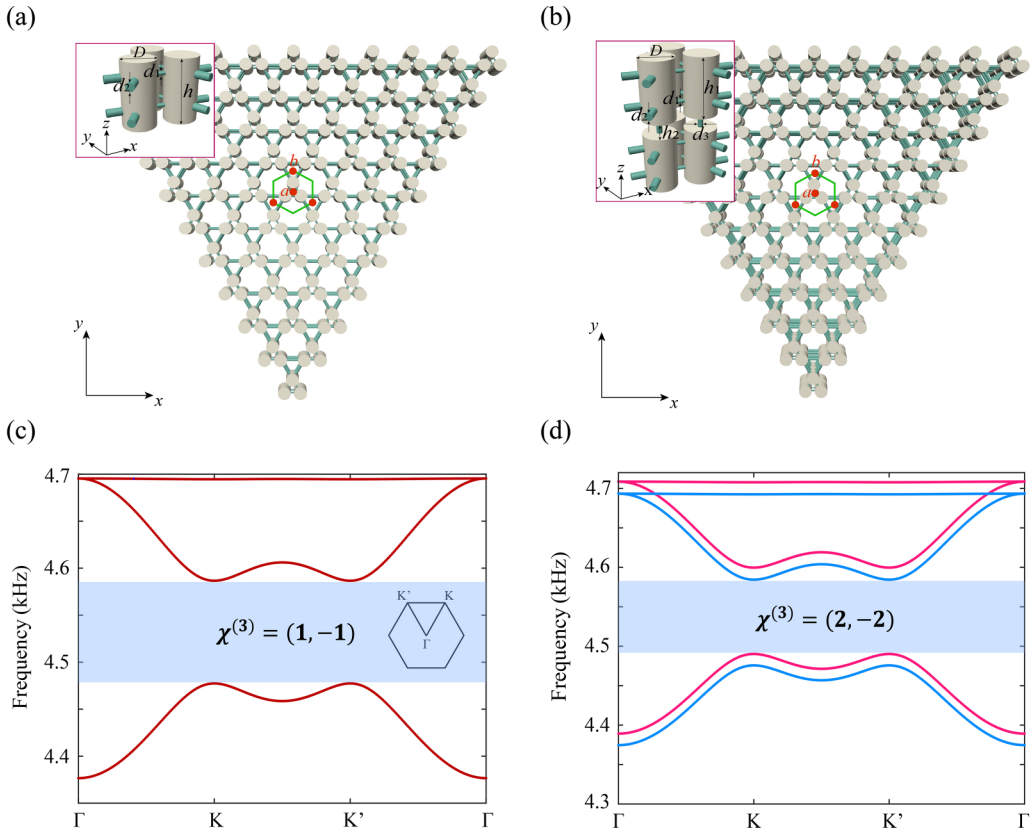

FIG. 8. (a) Schematic of monolayer phononic crystals with $h_{1b}^{(3)}$ configuration. Inset: The side view of the unit cell. (b) The mirror-stacked bilayer phononic crystals formed by two identical monolayer phononic crystals configured with $h_{1b}^{(3)}$ configuration. (c) Band structure of monolayer phononic crystals. (d) Band structure of the mirror-stacked bilayer phononic crystals with $h_{1b}^{(3)}$ configuration.

can move continuously into and out of the two-dimensional bulk continuum of opposite parity by tuning the interlayer couplings, which contribute topological bound states in the continuum.

To this end, we plot the energy spectra of the finite-sized mirror-stacked bilayer phononic crystals made up by monolayer phononic crystals configured with the upward kagome lattice versus the diameter of the interlayer connecting air tubes in Fig. 9(a). The shadow light blue (red) area and blue (red) line refer to the bulk (edge) and corner states of mirror-stacked bilayer phononic crystals with even (odd) parity, respectively. For each subspace, it is clearly seen that the corner states emerge as the manifestation of the higher-order band topology. Moreover, the corner states with odd (even) parity fall into the frequency windows of the bulk states with even (odd) parity when the diameter d_3 ranges from 1.2 mm (2.0 mm) to 4.6 mm (4.2 mm). Remarkably, since those energetically degenerate bound and continuum states (see the overlapped areas) belong to the subspaces of different parties, hence, hybridization cannot occur between them and yield the formation of the topological bound states in the continuum.

To verify it, Figs. 9(b)–9(d) display the band structures of the mirror-stacked bilayer phononic crystals with various diameters $d_3 = 1.2, 3.6, 5.0$ mm, respectively. As expected, the band offset between the bandsets with even and odd mirror parities widens, and the bandset with odd (even) mirror parity moves upwards (downwards) accompanying the increase of the interlayer couplings. Accordingly, we further present the eigenspectrum of mirror-stacked bilayer phononic crystals with finite-sized systems in Figs. 9(e)–9(g). Note that the eigenstates with even and odd mirror parities are separately plotted, as indicated by the blue and red points. It is seen that due to the lack of the chiral symmetry the corner states are no longer pinned at the center of the bulk gap. As shown in Fig. 9(e), when $d_3 = 1.2$ mm, the corner states at a frequency of $f_2 = 4547$ Hz with odd parity enter into the frequency range of the edge states with even parity, yielding the bound states in the edge. Meanwhile, the frequency of the corner state at a frequency of $f_1 = 4531$ Hz with even parity is in the frequency gap of the bandset with odd parity. The corresponding acoustic field patterns can be visualized in Fig. 10(a). For $d_3 = 3.6$ mm in Fig. 9(f), the corner states at a frequency of $f_1 = 4514$ Hz ($f_2 = 4624$ Hz) with even (odd) parities move to the frequency range of bulk states with odd (even) parity, yielding the topological bound states in the continuum, which can be visualized more clearly in the dashed boxes in Fig. 10(b). Further increasing d_3 to 5.0 mm [see the eigenspectrum in Fig. 9(g)], the corner states at a frequency of $f_1 = 4496$ Hz ($f_2 = 4702$ Hz) with even (odd) parity move away from the frequency windows of the bandset with odd (even) parity, leading to the disappearance of the topological bound states in the continuum [see the acoustic field pattern of the corner states with even and odd parities in Fig. 10(c)].

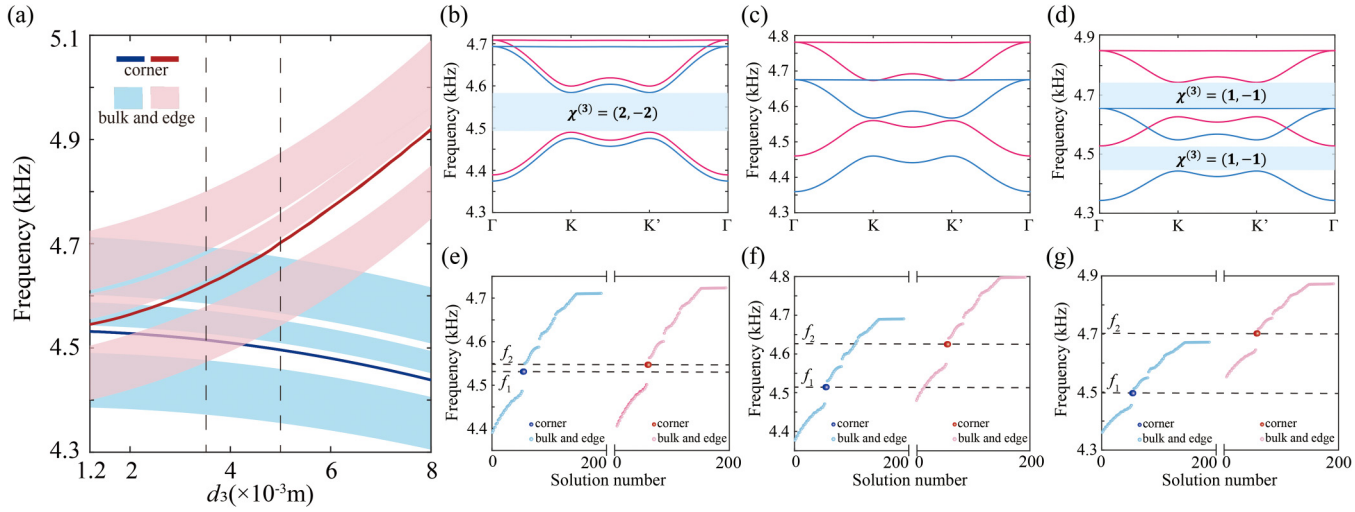

FIG. 9. (a) The eigenspectrum of mirror-stacked bilayer phononic crystals vs the diameter d_3 of the layer connecting tubes. (b)–(d) The band structure of the mirror-stacked bilayer phononic crystals with the diameter d_3 of the layer connecting tubes (b) $d_3 = 1.2$ mm, (c) $d_3 = 3.6$ mm, and (d) $d_3 = 5.0$ mm. (e)–(g) The corresponding eigenspectrum of the mirror-stacked bilayer phononic crystals in (b)–(d), where the blue and red points refer to the acoustic states with even and odd mirror parities, respectively.

D. C_3-symmetric mirror-stacked bilayer phononic crystals formed by a downward kagome lattice ($h_{1c}^{(3)}$ and $h_{1c}^{(3)}$)

It is noteworthy that there exists another C_3-symmetric lattice. As shown in Fig. 11(a), each unit cell is made up by three cavity resonators, which are aligned with downward triangular shape. For simplicity, we denote it as the downward kagome lattice. Note that the geometric parameters of monolayer phononic crystals in downward kagome lattice configuration are the same as those of the upward kagome lattice. Hence, it is evident that the monolayer phononic crystals in downward kagome lattice configuration share the same band structure with that of the upward kagome lattice, which is depicted in Fig. 11(c). Nevertheless, we also remark that the topological indices of monolayer phononic crystals in downward kagome lattice configuration are $\chi^{(3)} = (1, 0)$, which are different from those of the upward kagome lattice. In view of the Wannier configuration, the Wannier center of the lowest band is located at position c [also see the green hexagon in Fig. 11(a)]. Hence, the monolayer with downward kagome lattice is of $h_{1c}^{(3)}$ configuration. Accordingly, the fractional corner charge arising from the filling anomaly via Eq. (5) is zero.

Next, we further construct C_3-symmetric mirror-stacked bilayer phononic crystals by stacking two identical monolayer phononic crystals in downward kagome lattice configuration, as indicated in Fig. 11(b). The diameter of the connecting air tube between two layers is given by d_3. Figure 11(d) depicts the band structure of the mirror-stacked bilayer phononic

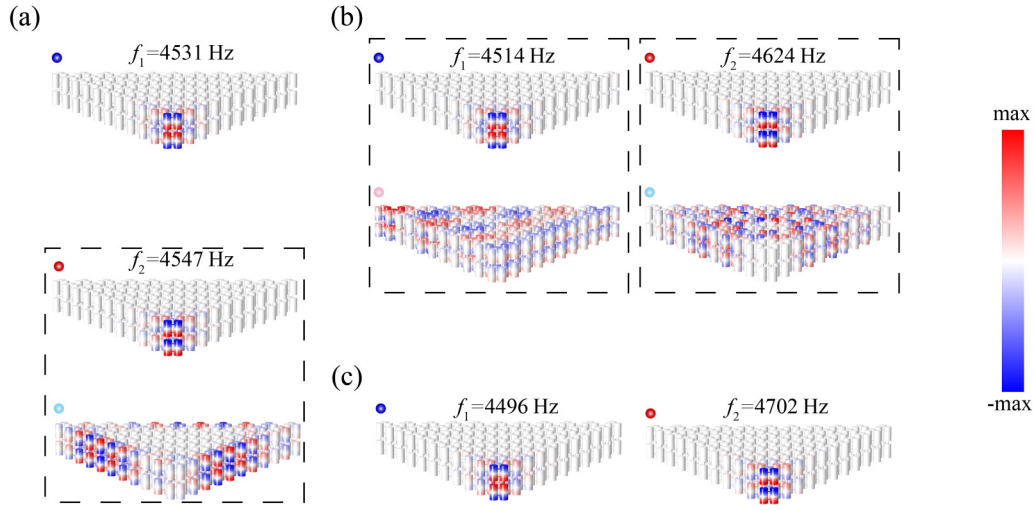

FIG. 10. (a)–(c) The corresponding acoustic pressure field pattern of mirror-stacked bilayer phononic crystals with (a) $d_3 = 1.2$ mm at frequencies of $f_1 = 4531$ Hz and $f_2 = 4547$ Hz, (b) $d_3 = 3.6$ mm at frequencies of $f_1 = 4514$ Hz and $f_2 = 4624$ Hz, and (c) $d_3 = 5.0$ mm, at frequencies of $f_1 = 4496$ Hz and $f_2 = 4702$ Hz, respectively. The topological bound states in the continuum can be visualized from those acoustic pressure field patterns in the boxes.

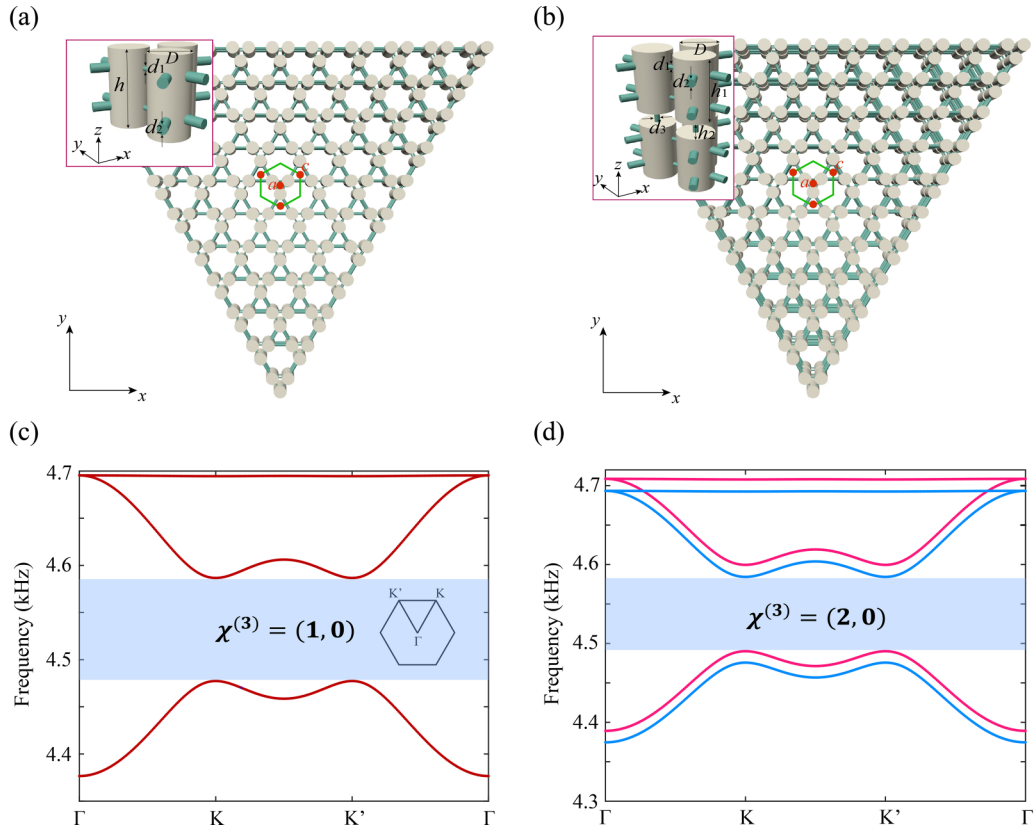

FIG. 11. (a) Schematic of monolayer phononic crystals in downward kagome lattice configuration. Inset: The side view of the primitive cell. (b) The mirror-stacked bilayer phononic crystals formed by two identical monolayers' phononic crystals. (c) Band structure of monolayer phononic crystals. (d) Band structure of the C_3-symmetric mirror-stacked bilayer phononic crystals in downward kagome lattice configuration.

crystals. As expected, they share the identical band structure of the monolayer and mirror-stacked bilayer phononic crystals with h_{1b} configuration. It is seen that there are six bands, which according to their mirror parities, can be divided into two sets. The blue (red) bandset refers to the bands with even (odd) mirror parity. Obviously, the interlayer coupling results in the splitting of the bands with odd and even parities. The calculated topological indices of the first gap give $\chi^{(3)} = (2, 0)$, which are the summation of topological indices of two identical monolayer phononic crystals, while the filling anomaly of the Wannier configuration results in zero fractional corner charge.

Owing to the higher-order band topology in the monolayer, it is evident that each layer structure with finite size supports three corner states in the gap. When two monolayers are placed together via mirror-stacking approach, each layer also hosts corner states that inherit higher-order band topology of the monolayer. Similar to the bulk band with specific mirror parity, six corner states in the gap are reorganized into two groups according to the mirror parities. Therefore, it is possible that the corner states can move continuously into and out of the two-dimensional bulk continuum of opposite parity by tuning the interlayer couplings, which contribute topological bound states in the continuum.

To this end, we plot the energy spectra of finite-sized mirror-stacked bilayer phononic crystals versus the diameter d_3 of the interlayer connecting air tube in Fig. 12(a). The shadow light blue (red) area and the blue (red) line refer to the bulk (edge) and corner states of mirror-stacked bilayer phononic crystals with even (odd) parity, respectively. For each subspace, it is clearly seen that a corner state emerges as the manifestation of the higher-order band topology. Moreover, the corner states with odd (even) parity fall into the frequency windows of the bulk states with even (odd) parity when the diameter d_3 ranges from 1.2 mm (1.6 mm) to 3.8 mm (5.0 mm). Remarkably, since those energetically degenerate bound and continuum states (see the overlapped areas) belong to the subspaces of different parties, hence, hybridization cannot occur between them and yielding the formation of the topological bound states in the continuum.

To verify it, Figs. 12(b)–12(d) display the band structures of the mirror-stacked bilayer phononic crystals with various diameters $d_3 = 1.2, 3.6, 5.0$ mm, respectively. As expected, the band offset between the bandset with even and odd mirror parities widens, and the bandset with odd (even) mirror parity moves upwards (downwards) accompanying the increase of the interlayer couplings. Accordingly, we further present the eigenspectrum of finite-sized mirror-stacked bilayer phononic crystals in Figs. 12(e)–12(g). Note that the eigenstates with even and odd mirror parities are separately plotted, as indicated by the blue and red points. It is seen that due to the lack of the chiral symmetry, the corner states are no longer pinned at the center of the bulk gap. As shown in Fig. 12(e), when $d_3 = 1.2$ mm, the corner states at a frequency of $f_2 = 4600$ Hz with odd parity fall into the frequency range of the bulk states with even parity, yielding the bound states in the

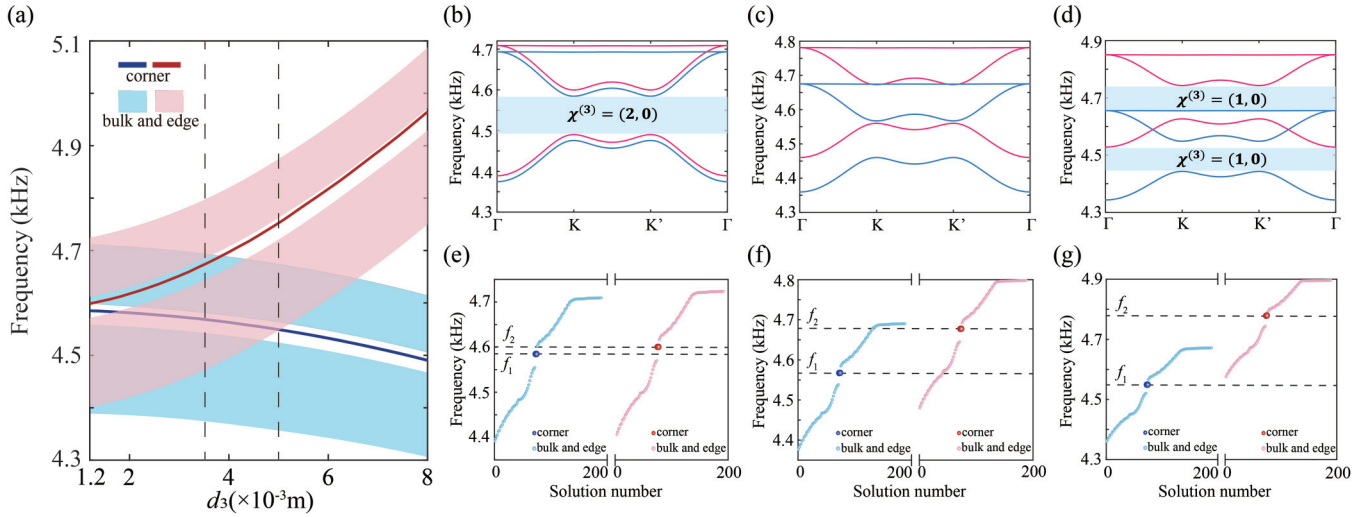

FIG. 12. (a) The eigenspectrum of mirror-stacked bilayer phononic crystals vs the interlayer coupling d_3. (b)–(d) The band structure of the mirror-stacked bilayer phononic crystals with interlayer coupling (b) $d_3 = 1.2$ mm, (c) $d_3 = 3.6$ mm, and (d) $d_3 = 5.0$ mm. (e)–(g) The corresponding eigenspectrum of the mirror-stacked bilayer phononic crystal in (b)–(d), where the blue and red points refer to the acoustic states with even and odd mirror parities, respectively.

continuum. Meanwhile, the corner state at a frequency of $f_1 = 4585$ Hz with even parity is in the frequency gap of the bandset with odd parity. The corresponding acoustic field pattern can be visualized in Fig. 13(a). For the case of $d_3 = 3.6$ mm in Fig. 12(f), the corner states at a frequency of $f_2 = 4678$ Hz ($f_1 = 4568$ Hz) with odd (even) parity fall into the frequency range of bulk states with even (odd) parity, yielding the topological bound states in the continuum, which can be visualized more clearly in the dashed boxes of Fig. 13(b). Further increasing d_3 to 5.0 mm [see Fig. 12(g)], the corner states at a frequency of $f_2 = 4752$ Hz ($f_1 = 4549$ Hz) with odd (even) parity move into the frequency gap of the bandset with even (odd) parity [see the acoustic field patterns in Fig. 13(c)].

To conclude this section, we emphasize that the interlayer coupling controlled by the diameter of the connecting air tubes in the mirror-stacked bilayer phononic crystals plays a vital role in the emergence of topological bound states in the continuum, and the topological corner and bulk states serve as bound and continuum states, respectively. To be specific, the mirror symmetry enables the separation of the Hilbert space and hence hinders the hybridization of the topological corner and bulk states with different mirror symmetry eigenvalues. Due to the independence of the two subspaces, the summation of the gap topological indices of mirror-stacked bilayer phononic crystals remains unchanged during the band evolutions.

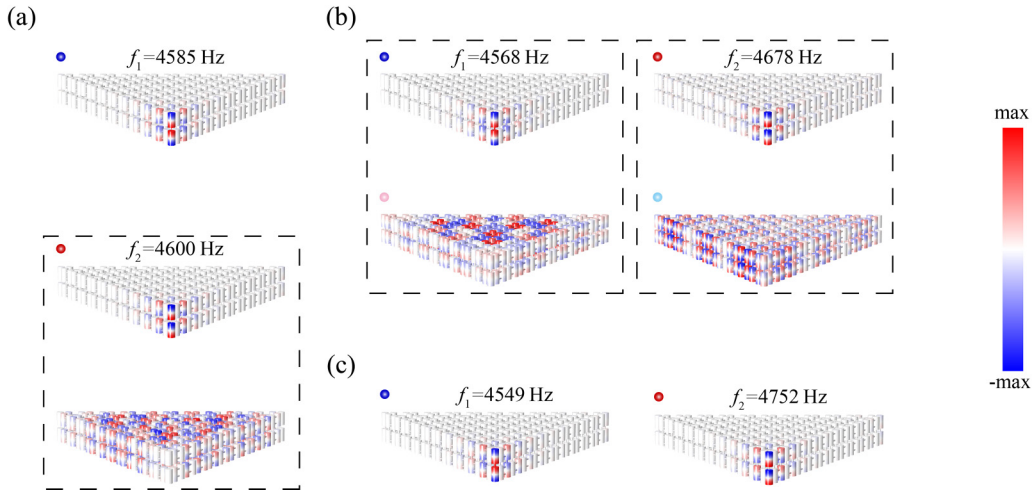

FIG. 13. (a)–(c) The corresponding acoustic pressure field pattern of mirror-stacked bilayer phononic crystals with (a) $d_3 = 1.2$ mm at frequencies of $f_1 = 4585$ Hz and $f_2 = 4600$ Hz, (b) $d_3 = 3.6$ mm at frequencies of $f_1 = 4568$ Hz and $f_2 = 4678$ Hz, and (c) $d_3 = 5.0$ mm at frequencies of $f_1 = 4549$ Hz and $f_2 = 4752$ Hz, respectively. The topological bound states in the continuum can be visualized from those acoustic pressure field patterns in the boxes.

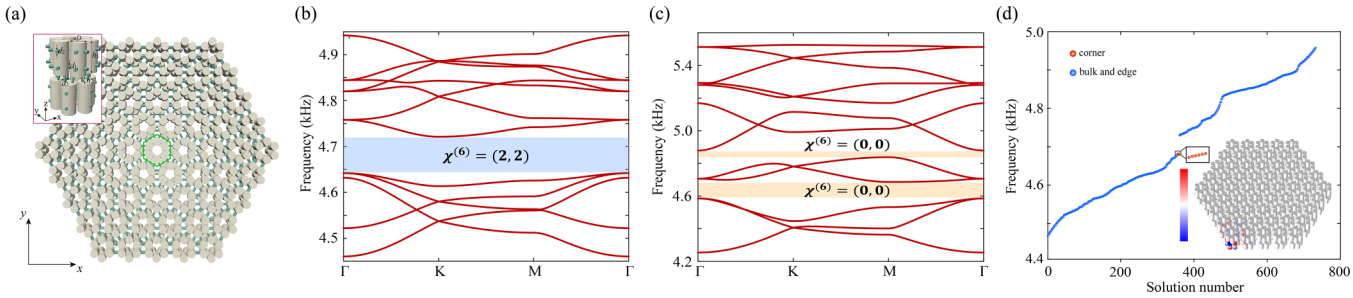

FIG. 14. (a) Top view of the C_6-symmetric heterogeneous-stacked bilayer phononic crystals, which formed by connecting the monolayer phononic crystal arrayed with Wu-Hu's and hexagonal lattices ($h_{2b}^{(6)}$ and $h_{3c}^{(6)}$), respectively. Inset: The unit cell. The geometric parameters of two monolayer phononic crystals are adopted from Figs. 2(a) and 5(a), respectively. The diameter of the individual cavity is $D = 18$ mm (b, c) Simulated band structure of heterogeneous-stacked bilayer phononic crystals with (b) weak interlayer coupling, i.e., $d_3 = 1.2$ mm, and (c) strong interlayer coupling, i.e., $d_3 = 8.0$ mm. (d) Eigenspectrum of the C_6-symmetric heterogeneous-stacked bilayer phononic crystals with $d_3 = 1.2$ mm. Inset: Simulated acoustic pressure profile of the corner state.

III. HETEROGENEOUS-STACKED BILAYER PHONONIC CRYSTALS

Based on the above studies, we further discuss the heterogeneous-stacked bilayer phononic crystals formed by stacking two different monolayer phononic crystals in this section. In general, there are at least two categories of heterogeneous-stacked bilayer phononic crystals according to the geometric symmetry. The first kind of heterogeneous-stacked bilayer phononic crystals is formed by stacking two different monolayer phononic crystals with identical symmetries, and the other kind of heterogeneous-stacked bilayer phononic crystals is formed by stacking two different monolayer phononic crystals with different symmetries.

A. C_6-symmetric heterogeneous-stacked bilayer phononic crystals formed by Wu-Hu's and hexagonal lattices ($h_{3c}^{(6)}$ and $h_{2b}^{(6)}$)

We first consider the C_6-symmetric heterogeneous-stacked bilayer phononic crystals formed by stacking Wu-Hu's and hexagonal lattices with nontrivial band topology. To this end, we adopt the monolayer phononic crystals configured with $h_{3c}^{(6)}$ and $h_{2b}^{(6)}$, and the geometric parameters are the same as in Figs. 2(a) and 5(a), respectively. As shown in Fig. 14(a), the unit cell indicated by the green hexagon consists of 12 acoustic cavities, and each cavity is connected with two nearest neighbor cavities (within the unit cell) of the upper or lower layer via two sloped air tubes. In what follows, we pay special attention to the role of the interlayer couplings on the band topological transition. We select two values of d_3, i.e., $d_3 = 1.2$ and 8 mm, which represent the weak and strong interlayer couplings, respectively, and present the corresponding band structure in Figs. 14(b) and 14(c), respectively.

For the C_6-symmetric heterogeneous-stacked bilayer phononic crystals with weak interlayer coupling, namely $d_3 = 1.2$ mm, in Fig. 14(b), it is seen that a band gap divides the 12 bands into two sets, the lower bandset below the gap consisting of five bands, with higher bandset above the gap consisting of seven bands. The lower bandset is inherited from the band structure of the monolayer phononic crystals, which is almost not affected. Nevertheless, due to the absence of the mirror symmetry, the separability into subspaces with opposite parities is no longer valid in heterogeneous-stacked bilayer phononic crystals, which is in strong contrast to that in the C_6-symmetric mirror-stacked bilayer phononic crystals. The band mixing effect originated from interlayer coupling can be further examined from the band anticrossing in the higher bandset. Note that the band gap of monolayer phononic crystals in the configuration of Wu-Hu's and hexagonal lattices shares a common frequency range, which, however, is of different nontrivial topology. Thanks to the compatible symmetry between Wu-Hu's and hexagonal lattices, it is possible to characterize the band topology of heterogeneous-stacked bilayer phononic crystals by utilizing the topological crystalline index. The calculated topological indices of the band gap give $\chi^{(6)} = (2, 2)$, suggesting a nontrivial higher-order topology. According to Eq. (3), the filling anomaly of the heterogeneous-stacked bilayer phononic crystals results in a fractional corner charge of $\frac{5}{6}$. Interestingly, the topological indices of the band gap in heterogeneous-stacked bilayer phononic crystals with weak interlayer coupling are equal to the summation of those in two monolayer phononic crystals. In other words, in the condition of weak interlayer coupling, the band topology of the heterogeneous-stacked bilayer phononic crystals inherits from the nontrivial monolayer phononic crystals.

For the C_6-symmetric heterogeneous-stacked bilayer phononic crystals with the strong interlayer coupling, namely $d_3 = 8$ mm, in Fig. 14(c), it is seen that two band gaps divide the 12 bands into three sets. To be specific, the lowest bandset (with three bands) inherits the band structure of the monolayer phononic crystal configured with Wu-Hu's lattice, while higher bandsets are reorganized owing to the strong interlayer coupling, which is different from the condition of weak interlayer coupling. Remarkably, the calculated topological indices of both band gaps give $\chi^{(6)} = (0, 0)$, leading to the zero fractional corner charge. Hence, it is emphasized that the phase transition in the heterogeneous-stacked bilayer phononic crystals can be triggered by adjusting the interlayer couplings, rather than breaking the geometric symmetry. Generally, the topological phase transition is accompanied by the process of band gap closing and reopening, and the number of the bands below the band gap remains unchanged. However, the strong interlayer coupling leads to the band reorganization, which changes the number of the bands below the band gap. Hence, it is noteworthy that there is no specific transition point

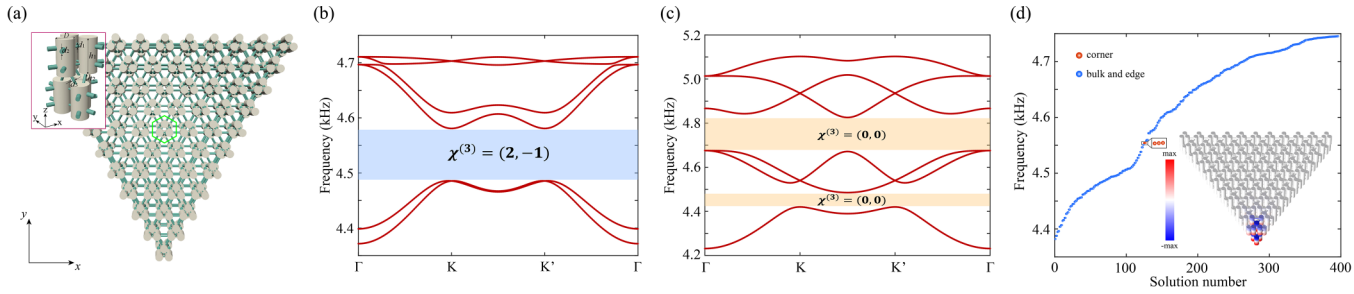

FIG. 15. (a) Top view of the C_3-symmetric heterogeneous-stacked bilayer phononic crystals, which formed by connecting the monolayer phononic crystal configured with Wu-Hu's and hexagonal lattices. Inset: The unit cell. The geometric parameters of two monolayer phononic crystals are adopted from Figs. 8(a) and 11(a), respectively. (b), (c) Simulated band structure of heterogeneous-stacked bilayer phononic crystals with (b) weak interlayer coupling, i.e., $d_3 = 1.2$ mm, and (c) strong interlayer coupling, i.e., $d_3 = 8.0$ mm. (d) Eigenspectrum of the C_3-symmetric heterogeneous-stacked bilayer phononic crystals with $d_3 = 1.2$ mm. Inset: Simulated acoustic pressure profile of the corner state.

during the topological phase transition triggered by interlayer couplings (see details in Appendix A).

To manifest the higher-order topology of C_6-symmetric heterogeneous-stacked bilayer phononic crystals, we construct a finite-sized heterogeneous-stacked bilayer phononic crystal [see Fig. 14(a)] and calculate its eigenspectrum with both weak and strong interlayer couplings. For heterogeneous-stacked bilayer phononic crystals with weak interlayer coupling, i.e., $d_3 = 1.2$ mm, as expected, six corner states marked by red points are identified at $f = 4682$ Hz in the nontrivial band gap in Fig. 14(d). The corresponding acoustic pressure field distributions are displayed in the inset of Fig. 14(d). Interestingly, since most of the acoustic pressure field is localized in the lower monolayer phononic crystal configured with Wu-Hu's lattice, it is believed that the nontrivial topology mostly originated from the monolayer phononic crystal in Wu-Hu's lattice configuration. Moreover, we remark that the interlayer coupling plays a key role in the topological phase transition in C_6-symmetric heterogeneous-stacked bilayer phononic crystals formed by both trivial and nontrivial monolayer phononic crystals, as we discuss in Appendix B.

B. C_3-symmetric heterogeneous-stacked bilayer phononic crystals formed by upward and downward kagome lattices ($h_{1b}^{(3)}$ and $h_{1c}^{(3)}$)

Following the above procedure, we now consider C_3-symmetric heterogeneous-stacked bilayer phononic crystals formed by stacking the monolayer phononic crystals configured with upward and downward kagome lattices, and the geometric parameters are adopted from Figs. 8(a) and 11(a). As shown in Fig. 15(a), the unit cell indicated by the green hexagon consists of six acoustic cavities, and each cavity is connected with two nearest neighbor cavities (within the unit cell) of the upper or lower layer via two sloped air tubes. In what follows, we pay special attention to the role of the interlayer couplings on the topological transition. We select two values of d_3, i.e., $d_3 = 1.2$ and 8 mm, which represent the weak and strong interlayer couplings, and present their band structures in Figs. 15(b) and 15(c), respectively.

For the C_3-symmetric heterogeneous-stacked bilayer phononic crystals with weak interlayer coupling, namely $d_3 = 1.2$ mm, in Fig. 15(b), it is seen that a band gap divides the six bands into two sets; the lower bandset below the gap consists of two bands, while the higher bandset above the gap consists of four bands. Interestingly, the band structure of the C_3-symmetric heterogeneous-stacked bilayer phononic crystals can be regarded as the superposition of the band structure of the monolayer phononic crystals configured with upward and downward kagome lattices. Nevertheless, due to the absence of the mirror symmetry, the separability into subspaces with opposite parities is no longer valid in heterogeneous-stacked bilayer phononic crystals, which is in strong contrast to the C_3-symmetric mirror-stacked bilayer phononic crystals. Note that the monolayer phononic crystals in configurations of upward and downward kagome lattices share identical band gaps, which, however, are of different nontrivial topology. Thanks to the compatible symmetry between upward and downward kagome lattices, it is possible to characterize the band topology of heterogeneous-stacked bilayer phononic crystals by utilizing the topological crystalline index. The calculated topological indices of the band gap give $\chi^{(3)} = (2, -1)$, leading to a fractional charge of $\frac{2}{3}$. Interestingly, the topological indices of the band gap in heterogeneous-stacked bilayer phononic crystals with weak interlayer coupling are equal to the summation of those in two monolayer phononic crystals. In other words, in the condition of weak interlayer coupling, the band topology of the heterogeneous-stacked bilayer phononic crystals inherits from the nontrivial monolayer phononic crystals.

For the C_3-symmetric heterogeneous-stacked bilayer phononic crystals with strong interlayer coupling, namely $d_3 = 8$ mm, in Fig. 15(c), it is seen that two band gaps divide the six bands into three bandsets. To be specific, there is only a single band below the first band gap, while higher bandsets are reorganized owing to the strong interlayer coupling, which is different from weak interlayer coupling. Remarkably, the calculated topological indices of both band gaps give $\chi^{(3)} = (0, 0)$, leading to the zero fractional corner charge. Hence, it is emphasized that the phase transition in the C_3-symmetric heterogeneous-stacked bilayer phononic crystals can be triggered by adjusting the interlayer couplings, rather than breaking the geometric symmetry. Generally, the topological phase transition is accompanied by the process of band gap closing and reopening, and the number of the bands below the band gap remains unchanged. However, the

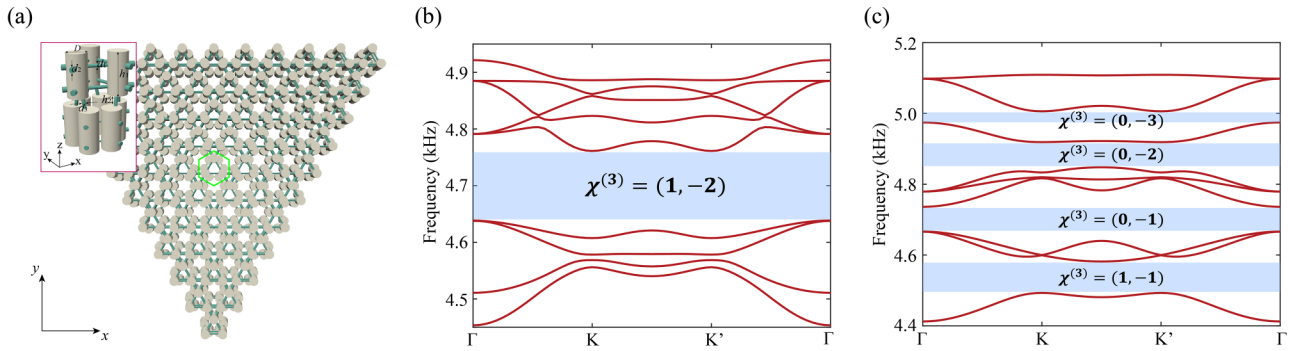

FIG. 16. (a) Top view of the C_3-symmetric heterogeneous-stacked bilayer phononic crystals, which formed by connecting the monolayer phononic crystal configured with Wu-Hu's and hexagonal lattices. Inset: The unit cell. The geometric parameters of two monolayer phononic crystals are listed as follows: $d_1 = 3.0$ mm, $d_2 = 4.8$ mm for upper layer and $d_1 = 1.6$ mm, $d_2 = 4.0$ mm for lower layer, respectively. (b), (c) Simulated band structure of heterogeneous-stacked bilayer phononic crystals with (b) weak interlayer coupling, i.e., $d_3 = 1.2$ mm, and (c) strong interlayer coupling, i.e., $d_3 = 5.0$ mm.

strong interlayer coupling leads to the band reorganization, which changes the number of the bands below the band gap. Hence, it is noteworthy that there is no specific transition point during the topological phase transition triggered by interlayer couplings.

To manifest the higher-order topology of C_3-symmetric heterogeneous-stacked bilayer phononic crystals, we construct finite-sized C_3-symmetric heterogeneous-stacked bilayer phononic crystals [see Fig. 15(a)] and implement the eigencalculation in the condition of both weak and strong interlayer couplings. For C_3-symmetric heterogeneous-stacked bilayer phononic crystals with weak interlayer coupling, i.e., $d_3 = 1.2$ mm, as expected, three corner states marked by red points are identified at a frequency of $f = 4554$ Hz in the nontrivial band gap in Fig. 15(d). The corresponding acoustic pressure field distributions are displayed in the inset of Fig. 15(d).

C. C_3-symmetric heterogeneous-stacked bilayer phononic crystals formed by Wu-Hu's and downward kagome lattices ($h_{3c}^{(6)}$ and $h_{1b}^{(3)}$)

Although we consider heterogeneous-stacked bilayer phononic crystals formed by two different monolayer phononic crystals with identical symmetry, it is possible to construct heterogeneous-stacked bilayer phononic crystals (HSPCs) by stacking two different monolayer phononic crystals with distinct symmetry. As an illustration, we consider another C_3-symmetric heterogeneous-stacked bilayer phononic crystal formed by monolayer phononic crystals in configurations of upward kagome lattice and hexagonal lattice. The former lattice with C_3 symmetry is compatible with the latter with C_6 symmetry, making it possible to construct HSPCs. As shown in Fig. 16(a), the upper (lower) layer of the unit cell consists of three (six) acoustic cavities, and two monolayer phononic crystals are connected via three pairs of air tubes. In what follows, we pay special attention to the role of the interlayer couplings on the topological transition. We select two values of d_3, i.e., $d_3 = 1.2$ and 5 mm, which represent the weak and strong interlayer couplings, and present their band structures in Figs. 16(b) and 16(c), respectively.

For the C_3-symmetric heterogeneous-stacked bilayer phononic crystals with weak interlayer coupling, namely $d_3 = 1.2$ mm, in Fig. 16(b), it is seen that a band gap divides the nine bands into two sets; the lower bandset below the gap consists of four bands, while the higher bandset above the gap consists of five bands. Note that the band gaps of the monolayer phononic crystals in configurations of Wu-Hu's and upward kagome lattices share a common frequency range, which, however, are of different nontrivial topology. Thanks to the compatible symmetry between Wu-Hu's and upward kagome lattices, it is possible to characterize the band topology of heterogeneous-stacked bilayer phononic crystals by utilizing the topological crystalline index, which gives $\chi^{(3)} = (1, -2)$ and results in a fractional corner charge of $\frac{1}{3}$.

On the other hand, for the C_3-symmetric heterogeneous-stacked bilayer phononic crystals with strong interlayer coupling, namely $d_3 = 5$ mm, in Fig. 16(c), it is seen that only a single band is below the first band gap, while higher bandsets are reorganized owing to the strong interlayer coupling, which makes a difference from weak interlayer coupling. Remarkably, the calculated topological indices of all band gaps indicate that all band gaps are of topological nontrivial nature [see the calculated topological indices in Fig. 16(c)]. In contrast to the phase transition from topological nontrivial to trivial, here we identify that there exist topological transitions between two nontrivial phases in the C_3-symmetric heterogeneous-stacked bilayer phononic crystals. Generally, the topological phase transition is accompanied by the process of band gap closing and reopening, and the number of the bands below the band gap remains unchanged. However, the strong interlayer coupling leads to the band reorganization, which changes the number of the bands below the band gap. Hence, it is noteworthy that there is no specific transition point during the topological phase transition triggered by interlayer couplings.

To manifest the higher-order topology of C_3-symmetric heterogeneous-stacked bilayer phononic crystals, we construct finite-sized C_3-symmetric heterogeneous-stacked bilayer phononic crystals [see Fig. 16(a)] and implement the eigencalculation in the condition of both weak and strong interlayer couplings. For C_3-symmetric heterogeneous-stacked bilayer phononic crystals with weak interlayer coupling, i.e., $d_3 = 1.2$ mm, as expected, three corner states marked by red

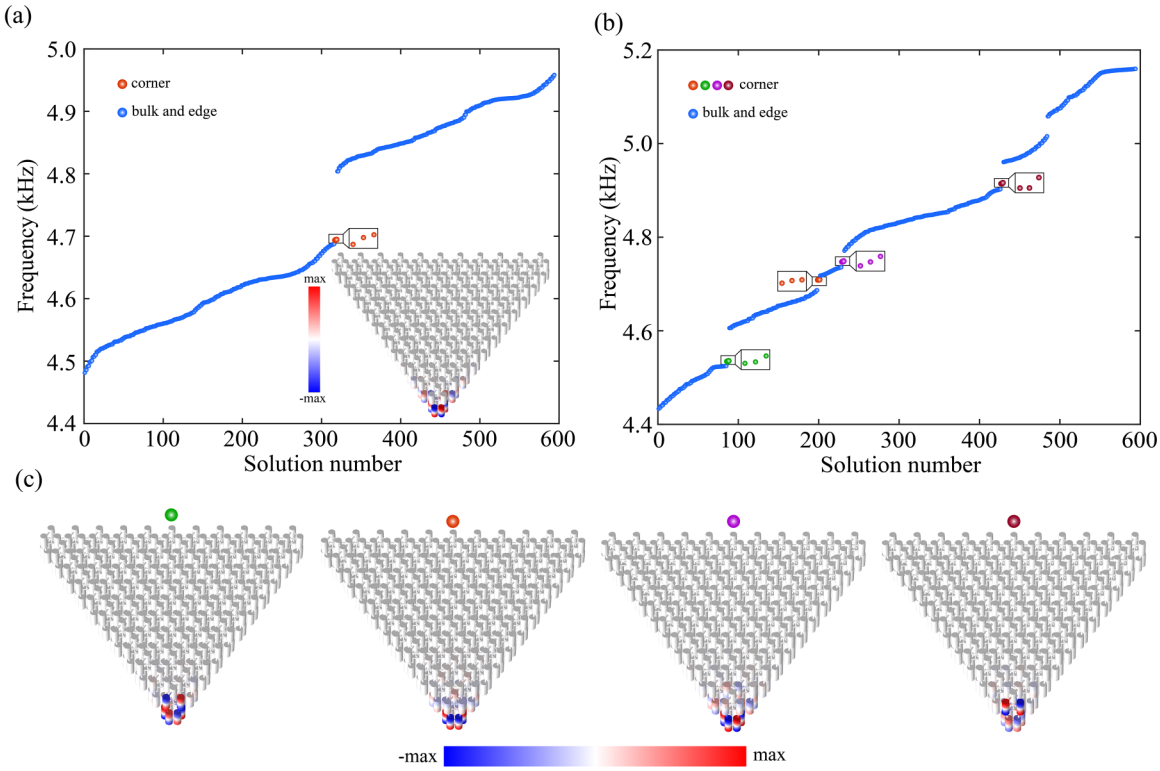

FIG. 17. Eigenspectrum of the C_3-symmetric heterogeneous-stacked bilayer phononic crystals with (a) weak interlayer coupling $d_3 = 1.2$ mm, where the inset refers to the acoustic profile of the corner state at a frequency of 4694 Hz and (b) strong interlayer coupling $d_3 = 5.0$ mm. (c) Simulated acoustic pressure profiles of the corner state marked in (b) at frequencies of 4535,4709, 4748, and 4918 Hz, respectively.

points are identified at $f = 4694$ Hz in the nontrivial band gap in Fig. 17(a). The corresponding acoustic pressure field distributions are displayed in the inset of Fig. 17(a). In contrast, for C_3-symmetric heterogeneous-stacked bilayer phononic crystals with strong interlayer coupling, namely, $d_3 = 5.0$ mm, there also exist four sets of corner states [see Fig. 17(b)]. Figure 17(c) further displays the corresponding acoustic pressure profiles of the corner states.

Last but not least, it is noteworthy that the nontrivial band topology of heterogeneous-stacked bilayer phononic crystals is inherited from monolayer phononic crystals, while the interlayer coupling provides an alternative way to trigger the topological phase transition. In other words, it is impossible to realize phase transition if the heterogeneous-stacked bilayer phononic crystals are formed by two trivial monolayer phononic crystals (see details in Appendix C).

IV. CONCLUSION AND DISCUSSIONS

In conclusion, we systematically studied the C_6- and C_3-symmetric higher-order topological phases in bilayer phononic crystals with two types of stackings: the mirror symmetric stacking and the heterogeneous stacking. For the mirror-stacked bilayer lattice, the separability of the Hilbert space with odd and even parities and the tuning of the interlayer coupling enable the emergence and disappearance of the topological corner states in the bulk continuum. For the bilayer phononic crystals formed by two distinct monolayer lattices of the same symmetry, the band topology is strongly affected by the interlayer couplings as well as the two original monolayers. The bilayer phononic crystals can even experience a phase transition from nontrivial to trivial band topology when the interlayer coupling is gradually strengthened. Our paper unveil the rich physics of the interlayer couplings in bilayer systems, suggesting that the layer degree of freedom can be used to enrich the higher-order topological phases.

ACKNOWLEDGMENTS

This work was supported by the National Key Research and Development Program of China (Grant No. 2022YFA1404400), the National Natural Science Foundation of China (Grants No. 12125504, No. 11904060, No. 12074281, and No. 12204417), the "Hundred Talents Program" of the Chinese Academy of Sciences, the Natural Science Foundation of Guangxi Province (Grant No. 2023GXNSFAA026048), and the Priority Academic Program Development of Jiangsu Higher Education Institutions.

APPENDIX A: BAND EVOLUTION OF HETEROGENEOUS-STACKED BILAYER PHONONIC CRYSTALS WITH INCREASING INTERLAYER COUPLING

In most existing cases, the process of band gap closing and reopening is a hallmark of the topological phase transition. However, accompanying strong interlayer coupling, bands of heterogeneous-stacked bilayer phononic crystals originated from different lattices interacted with each other, resulting in the band reorganization, which may change the band number below the band gap. To prove it, we present the

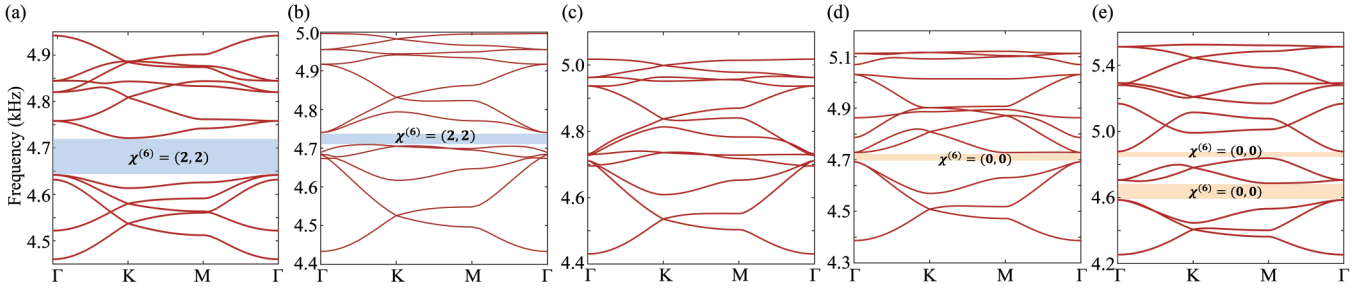

FIG. 18. Band structures of C_6-symmetric heterogeneous-stacked bilayer phononic crystals formed by monolayer phononic crystals in configuration of Wu-Hu's and hexagonal lattices with (a) $d_3 = 1.2$ mm, (b) $d_3 = 3.4$ mm, (c) $d_3 = 3.8$ mm, (d) $d_3 = 6.0$ mm, and (e) $d_3 = 8.0$ mm.

band structures of C_6-symmetric heterogeneous-stacked bilayer phononic crystals with various d_3 in Fig. 18. Let us focus on the first band gap; for C_6-symmetric heterogeneous-stacked bilayer phononic crystals, it is seen that there are five bands below the first band gap for C_6-symmetric heterogeneous-stacked bilayer phononic crystals with $d_3 = 1.2$ and 3.4 mm, of which the topological indices are $\chi^{(6)} = (2, 2)$. On the other hand, only three bands are below the first band gap for C_6-symmetric heterogeneous-stacked bilayer phononic crystals with $d_3 = 6.0$ and 8.0 mm, of which the topological indices are $\chi^{(6)} = (0, 0)$. Obviously, it is impossible to identify the specific transition point.

APPENDIX B: C_6-SYMMETRIC HETEROGENEOUS-STACKED BILAYER PHONONIC CRYSTALS FORMED BY TRIVIAL AND NONTRIVIAL MONOLAYER PHONONIC CRYSTALS

Here we consider the heterogeneous-stacked bilayer phononic crystals formed by trivial and nontrivial monolayer phononic crystals, and pay special attention to the role of the interlayer couplings. As shown in Fig. 19(a), we construct C_6-symmetric heterogeneous-stacked bilayer phononic crystals by stacking Wu-Hu's lattice with $d_1 = 1.6$ mm and $d_2 = 4.2$ mm, and the hexagonal lattice with trivial configuration, i.e., $d_1 = 2.4$ mm and $d_2 = 2.6$ mm. By setting the interlayer coupling strength $d_3 = 0.8$ and 6.0 mm, which represent weak and strong couplings, respectively, we discuss the interlayer coupling effect on the phase transition. The band structures are displayed in Figs. 19(b) and 19(c), and the gap topological indices are $\chi^{(6)} = (2, 0)$ and (0,0), indicating that the strong interlayer coupling triggers a phase transition.

To manifest the nontrivial band topology in the heterogeneous-stacked bilayer phononic crystals, we construct a finite-sized heterogeneous-stacked bilayer phononic crystal and calculate its eigenspectrum. The results are displayed in Fig. 19(d). It is seen that the corner states, as the hallmark of the higher-order topological phases, emerge in the band gaps. The simulated acoustic pressure profiles of the corner states are presented in inset of Fig. 19(d).

APPENDIX C: C_6-SYMMETRIC HETEROGENEOUS-STACKED BILAYER PHONONIC CRYSTALS FORMED BY STACKING MONOLAYER PHONONIC CRYSTALS WITH TRIVIAL BAND TOPOLOGY

In the main text, we only focus on the bilayer phononic crystal formed by stacking nontrivial monolayer phononic crystals. It should be emphasized that the band topology of the heterogeneous-stacked bilayer phononic crystals, if present, is originated from the higher-order topological monolayer phononic crystals. In other words, the trivial monolayer phononic crystals cannot generate nontrivial topological heterogeneous-stacked bilayer phononic crystals no matter how the interlayer coupling is tuned. To verify it, here we consider the heterogeneous-stacked bilayer phononic crystals formed by monolayer phononic crystals in configuration of Wu-Hu's and hexagonal lattices

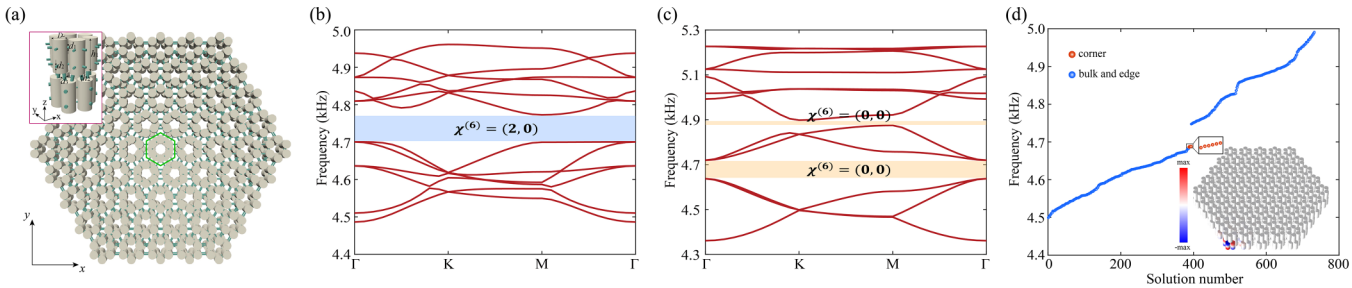

FIG. 19. (a) Schematic of C_6-symmetric heterogeneous-stacked bilayer phononic crystals formed by stacking the both trivial (upper layer) and nontrivial monolayers (bottom layer). Inset: The primitive cell. (b, c) Band structures of C_6-symmetric heterogeneous-stacked bilayer phononic crystals with (b) $d_3 = 0.8$ mm and (c) $d_3 = 6.0$ mm. (d) Eigenspectrum of C_6-symmetric finite-sized heterogeneous-stacked bilayer phononic crystals with $d_3 = 0.8$ mm and its acoustic pressure profiles of the corner states.

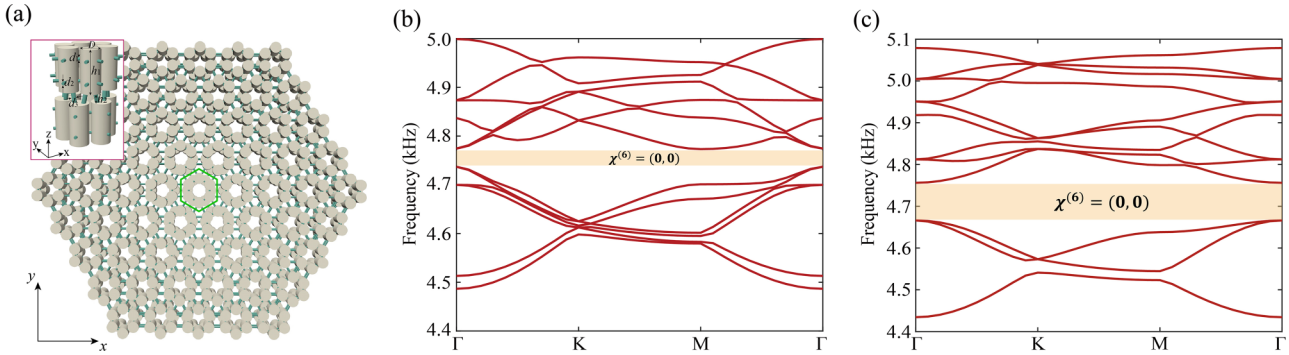

FIG. 20. (a) Schematic of C_6-symmetric heterogeneous-stacked bilayer phononic crystals formed by two trivial monolayer phononic crystals. (b, c) Eigenspectrum of the heterogeneous-stacked bilayer phononic crystals with (b) weak interlayer coupling $d_3 = 0.8$ mm and (c) strong interlayer coupling $d_3 = 4.0$ mm.

with trivial band topology [see Fig. 20(a)]. The geometric parameters are listed as follows: $d_1 = 2.6$ mm, $d_2 = 2.8$ mm. To examine the interlayer coupling effect on the band topology of heterogeneous-stacked bilayer phononic crystals, we select $d_3 = 0.8$ mm ($d_3 = 4.0$ mm) to mimic the weak (strong) interlayer couplings, and calculate the corresponding topological indices. The band structures of heterogeneous-stacked bilayer phononic crystals with weak and strong interlayer coupling are displayed in Figs. 20(b) and 20(c), respectively. It is seen that both heterogeneous-stacked bilayer phononic crystals exhibit a complete band gap, and the calculated topological indices of both band gaps are $\chi^{(6)} = (0, 0)$, indicating that they are of trivial topology.

[1] X. Zhang, M. Xiao, Y. Cheng, M.-H. Lu, and J. Christensen, Topological sound, Commun. Phys. **1**, 97 (2018).

[2] G. Ma, M. Xiao, and C. T. Chan, Topological phases in acoustic and mechanical systems, Nat. Rev. Phys. **1**, 281 (2019).

[3] Y. Liu, X. Chen, and Y. Xu, Topological phononics: From fundamental models to real materials, Adv. Funct. Mater. **30**, 1904784 (2020).

[4] H. Xue, Y. Yang, and B. Zhang, Topological acoustics, Nat. Rev. Mater. **7**, 974 (2022).

[5] Z.-K. Lin and J.-H. Jiang, Dirac cones and higher-order topology in quasi-continuous media, Europhys. Lett. **137**, 15001 (2022).

[6] X. Zhang, F. Zangeneh-Nejad, Z.-G. Chen, M.-H. Lu, and J. Christensen, A second wave of topological phenomena in photonics and acoustics, Nature (London) **618**, 687 (2023).

[7] B. Xie, H.-X. Wang, X. Zhang, P. Zhan, J.-H. Jiang, M. Lu, and Y. Chen, Higher-order band topology, Nat. Rev. Phys. **3**, 520 (2021).

[8] W. A. Benalcazar, B. A. Bernevig, and T. L. Hughes, Quantized electric multipole insulators, Science **357**, 61 (2017).

[9] M. Serra-Garcia, V. Peri, R. Süsstrunk, O. R. Bilal, T. Larsen, L. G. Villanueva, and S. D. Huber, Observation of a phononic quadrupole topological insulator, Nature (London) **555**, 342 (2018).

[10] X. Zhang, Z.-K. Lin, H.-X. Wang, Z. Xiong, Y. Tian, M.-H. Lu, Y.-F. Chen, and J.-H. Jiang, Symmetry-protected hierarchy of anomalous multipole topological band gaps in nonsymmorphic metacrystals, Nat. Commun. **11**, 65 (2020).

[11] Y. Qi, C. Qiu, M. Xiao, H. He, M. Ke, and Z. Liu, Acoustic realization of quadrupole topological insulators, Phys. Rev. Lett. **124**, 206601 (2020).

[12] X. Ni, M. Li, M. Weiner, A. Alù, and A. B. Khanikaev, Demonstration of a quantized acoustic octupole topological insulator, Nat. Commun. **11**, 2108 (2020).

[13] H. Xue, Y. Ge, H.-X. Sun, Q. Wang, D. Jia, Y.-J. Guan, S.-Q. Yuan, Y. Chong, and B. Zhang, Observation of an acoustic octupole topological insulator, Nat. Commun. **11**, 2442 (2020).

[14] M. Ezawa, Higher-order topological insulators and semimetals on the breathing kagome and pyrochlore lattices, Phys. Rev. Lett. **120**, 026801 (2018).

[15] X. Zhang, H.-X. Wang, Z.-K. Lin, Y. Tian, B. Xie, M.-H. Lu, Y.-F. Chen, and J.-H. Jiang, Second-order topology and multidimensional topological transitions in sonic crystals, Nat. Phys. **15**, 582 (2019).

[16] X. Ni, M. Weiner, A. Alù, and A. B. Khanikaev, Observation of higher-order topological acoustic states protected by generalized chiral symmetry, Nat. Mater. **18**, 113 (2019).

[17] M. Ezawa, Minimal models for Wannier-type higher-order topological insulators and phosphorene, Phys. Rev. B **98**, 045125 (2018).

[18] X. Zhang, L. Liu, M.-H. Lu, and Y.-F. Chen, Valley-selective topological corner states in sonic crystals, Phys. Rev. Lett. **126**, 156401 (2021).

[19] H. Xue, Y. Yang, G. Liu, F. Gao, Y. Chong, and B. Zhang, Realization of an acoustic third-order topological insulator, Phys. Rev. Lett. **122**, 244301 (2019).

[20] Y. Wu, M. Yan, Z.-K. Lin, H.-X. Wang, F. Li, and J.-H. Jiang, On-chip higher-order topological micromechanical metamaterials, Sci. Bull. **66**, 1959 (2021).

[21] S. Wu, B. Jiang, Y. Liu, and J.-H. Jiang, All-dielectric photonic crystal with unconventional higher-order topology, Photonics Res. **9**, 668 (2021).

[22] Z. Zhang, H. Long, C. Liu, C. Shao, Y. Cheng, X. Liu, and J. Christensen, Deep-subwavelength holey acoustic second-order topological insulators, Adv. Mater. **31**, 1904682 (2019).

[23] Z.-Z. Yang, Y.-Y. Peng, X. Li, X.-Y. Zou, and J.-C. Cheng, Boundary-dependent corner states in topological acoustic resonator array, Appl. Phys. Lett. **117**, 113501 (2020).

[24] S.-Q. Wu, Z.-K. Lin, B. Jiang, X. Zhou, Z. H. Hang, B. Hou, and J.-H. Jiang, Higher-order topological states in acoustic twisted Moiré superlattices, Phys. Rev. Appl. **17**, 034061 (2022).

[25] J. Li, Q. Mo, J.-H. Jiang, and Z. Yang, Higher-order topological phase in an acoustic fractal lattice, Sci. Bull. **67**, 2040 (2022).

[26] S. Zheng, X. Man, Z.-L. Kong, Z.-K. Lin, G. Duan, N. Chen, D. Yu, J.-H. Jiang, and B. Xia, Observation of fractal higher-order topological states in acoustic metamaterials, Sci. Bull. **67**, 2069 (2022).

[27] H.-X. Wang, Z.-K. Lin, B. Jiang, G.-Y. Guo, and J.-H. Jiang, Higher-order Weyl semimetals, Phys. Rev. Lett. **125**, 146401 (2020).

[28] L. Luo, H.-X. Wang, Z.-K. Lin, B. Jiang, Y. Wu, F. Li, and J.-H. Jiang, Observation of a phononic higher-order Weyl semimetal, Nat. Mater. **20**, 794 (2021).

[29] Q. Wei, X. Zhang, W. Deng, J. Lu, X. Huang, M. Yan, G. Chen, Z. Liu, and S. Jia, Higher-order topological semimetal in acoustic crystals, Nat. Mater. **20**, 812 (2021).

[30] L. Song, H. Yang, Y. Cao, and P. Yan, Square-root higher-order Weyl semimetals, Nat. Commun. **13**, 5601 (2022).

[31] Y. Zhang, C. Liu, X. Dai, and Y. Xiang, Coexisting hinge and vertical disclination states in a higher-order acoustic Dirac semimetal, Phys. Rev. B **107**, 214108 (2023).

[32] H. Qiu, M. Xiao, F. Zhang, and C. Qiu, Higher-order Dirac sonic crystals, Phys. Rev. Lett. **127**, 146601 (2021).

[33] L.-Y. Zheng and J. Christensen, Dirac hierarchy in acoustic topological insulators, Phys. Rev. Lett. **127**, 156401 (2021).

[34] L. Yang, Y. Wang, Y. Meng, Z. Zhu, X. Xi, B. Yan, S. Lin, J. Chen, B. J. Shi, Y. Ge, S. Q. Yuan, H. Chen, H. X. Sun, G. G. Liu, Y. Yang, and Z. Gao, Observation of Dirac hierarchy in three-dimensional acoustic topological insulators, Phys. Rev. Lett. **129**, 125502 (2022).

[35] S. Wang, H. Jia, X. Yang, P. Zhang, Y. Yang, Y. Yang, and X. Li, Realization of a full hierarchical topology in hexagonal bilayer acoustic crystals, Sci. China: Phys. Mech. Astron. **66**, 104311 (2023).

[36] C. He, H.-S. Lai, B. He, S.-Y. Yu, X. Xu, M.-H. Lu, and Y.-F. Chen, Acoustic analogues of three-dimensional topological insulators, Nat. Commun. **11**, 2318 (2020).

[37] C.-H. Xia, H.-S. Lai, X.-C. Sun, C. He, and Y.-F. Chen, Experimental demonstration of bulk-hinge correspondence in a three-dimensional topological Dirac acoustic crystal, Phys. Rev. Lett. **128**, 115701 (2022).

[38] J. Lu, C. Qiu, W. Deng, X. Huang, F. Li, F. Zhang, S. Chen, and Z. Liu, Valley topological phases in bilayer sonic crystals, Phys. Rev. Lett. **120**, 116802 (2018).

[39] H. Li, Z. Wang, Z. Wang, C. Deng, J. Luo, J. Huang, X. Wang, and H. Yang, Acoustic multichannel transports of valley edge states in bilayer sonic crystals, Appl. Phys. Lett. **121**, 243101 (2022).

[40] C. He, S.-Y. Yu, H. Ge, H. Wang, Y. Tian, H. Zhang, X.-C. Sun, Y. B. Chen, J. Zhou, M.-H. Lu, and Y.-F. Chen, Three-dimensional topological acoustic crystals with pseudospin-valley coupled saddle surface states, Nat. Commun. **9**, 4555 (2018).

[41] Y. Qi, H. Gao, T. Qin, J. Liang, W. Deng, X. Huang, J. Lu, and Z. Liu, Quadratic Dirac point and valley topological phases in acoustic analogues of AB-stacked bilayer graphene, Europhys. Lett. **134**, 37002 (2021).

[42] M. Gao, S. Wu, and J. Mei, Acoustic topological devices based on emulating and multiplexing of pseudospin and valley indices, New J. Phys. **22**, 013016 (2020).

[43] W. Deng, X. Huang, J. Lu, V. Peri, F. Li, S. D. Huber, and Z. Liu, Acoustic spin-Chern insulator induced by synthetic spin-orbit coupling with spin conservation breaking, Nat. Commun. **11**, 3227 (2020).

[44] S.-F. Li, A.-Y. Guan, C.-C. Wang, X.-Y. Zou, and J.-C. Cheng, Pseudospin-layer coupled edge states in an acoustic topological insulator, Appl. Phys. Lett. **122**, 262203 (2023).

[45] L. Liu, T. Li, Q. Zhang, M. Xiao, and C. Qiu, Universal mirror-stacking approach for constructing topological bound states in the continuum, Phys. Rev. Lett. **130**, 106301 (2023).

[46] Z. Pu, H. He, L. Luo, Q. Ma, L. Ye, M. Ke, and Z. Liu, Acoustic higher-order Weyl semimetal with bound hinge states in the continuum, Phys. Rev. Lett. **130**, 116103 (2023).

[47] W. A. Benalcazar, T. Li, and T. L. Hughes, Quantization of fractional corner charge in C_n-symmetric higher-order topological crystalline insulators, Phys. Rev. B **99**, 245151 (2019).

[48] L.-H. Wu and X. Hu, Scheme for achieving a topological photonic crystal by using dielectric material, Phys. Rev. Lett. **114**, 223901 (2015).